

POLITO - ETH - EPFL - PHELMA

Master degree course in Nanotechnologies for ICTs

Master Degree Thesis

**Development of a fully integrated
impedance-based platform for
in-vitro antischistosomal
pharmacodynamics analysis**



POLITECNICO
DI TORINO

ETH zürich

EPFL

Grenoble
phelma INP

Supervisors

Prof. Andreas Hierlemann
Prof. Danilo Demarchi
Dr. Mario Matteo Modena

Candidates

Francesco Grassi
ID number: 256890

Internship Tutor

Paolo Shayan Ravaynia

Academic Year 2019-2020

This work is subject to the Creative Commons Licence

Summary

Schistosomiasis is a tropical disease caused by a worm of the genus *Schistosoma* that infects around 230 million people worldwide, predominantly children living in poor rural areas of Sub-Saharan Africa. The demand for improving the identification of promising drugs is particularly high in the field of neglected tropical diseases, where funding and commercial investments are typically low. In addition to drug efficacy, information on pharmacodynamics is becoming tremendously urgent to enable the discovery of fast-acting compounds. Fast pharmacodynamic properties, low toxicity and long-lasting effects represent key parameters for the selection of highly promising compounds among potential leads during the *in vitro* screening process. A platform for *in-vitro* continuous dose-response characterization of drug candidates on *S. mansoni* larvae, using electrical impedance measurements to detect parasite viability, was recently released. As a further development, a supplementary drug wash-out assay for better *in vitro* selection prior to *in vivo* testing would be advantageous. An automated drug wash-out procedure would provide further insights on the efficacy of candidate compounds while still maintaining an adequate throughput for hit selection.

This thesis presents a portable integrated platform for additional pharmacodynamic analysis of drug candidates against *S. mansoni* larvae. A tubing-free microfluidic chip for antischistosomal drug wash-out assays, which addresses the limitations of manual procedures by drastically diminishing the operator effort and leaves open the possibility for continuous impedance-based viability evaluation, was designed. The timescale for drug removal was determined through a statistical analysis of pharmacokinetic data from a library of potential candidates. The platform design was optimized with the support of Comsol[®] simulations. Rapid prototyping techniques were adopted for chip fabrication, using almost exclusively thermoplastic polymers. The chip was validated in terms of flow profile and a suitability study was carried out to ensure the viability of *S. mansoni* larvae. In parallel, the requirements for a lock-in demodulator block for the impedance-based readout, which could be used for single-frequency impedance analysis at 500 kHz, were determined. The device thus selected performs similarly to the standard instrument and would drastically reduce the costs of the experimental test setups.

Finally, the results appear to be encouraging both for the microfluidic chip and for the readout platform. The early development parts were carried out successfully and will be the basis for future improvements in the context of parallelized high throughput screening on *S. mansoni*.

Contents

List of Figures

1	Introduction	1
1.1	Schistosomiasis overview	1
1.2	<i>S. mansoni</i> drug screening	3
1.3	Pharmacokinetics and Pharmacodynamics	5
1.4	Strategies for viability assessment of <i>S. mansoni</i>	6
1.5	EIS and NTS monitoring	8
1.6	Aim of the project	10
2	Materials and Methods	11
2.1	Experimental design	12
2.2	Statistical analysis of small compound half-life	12
2.3	Comsol simulations	14
2.4	Fabrication and workflow	15
2.4.1	Stacked Topology	15
2.4.2	Components Patterning	17
2.4.3	Assembly	19
2.4.4	Alternative approach: PDMS Chips	19
2.4.5	Loading procedure	20
2.4.6	Main challenge: capillary stop	20
2.5	Hydraulic resistance measurement setup	22
2.6	FITC Microscopy	24
2.7	NTS samples preparation	25
2.8	Extracted specifications for the demodulator block	26
2.9	Predictive simulations for demodulator components selection	28
2.10	EIS measurement setup	29
3	Results	35
3.1	Hydraulic resistance estimation	36
3.2	FITC concentration Measurements	36
3.3	Investigation of chip suitability for drug-washing assays on NTS	38
3.4	Impedance-based viability assessment of <i>S. mansoni</i> larvae	42

4 Discussion and conclusions	43
A Microfluidics	45
A.1 Fundamentals	46
A.2 Materials	48
A.3 Common issues	49
B Capillary effects	51
B.1 Surface Tension	51
B.2 Capillary Pressure	52
B.3 Contact angle	53
B.4 Impact on this work	55
C Demodulation	57
D Simulink models insights	59
E Comsol models insights	65
E.1 Sub-model I: preliminary information	66
E.2 From Model I to Model II	68
E.3 Model II: concentration profile	71
F Protocol for SU8 patterning	75
G Half-lives data collection	77
H SPICE simulations	81
Bibliography	83
List of abbreviations	87

List of Figures

1.1	<i>S. mansoni</i> life cycle [2] and NTS representation.	1
1.2	A: State-of-the-art <i>in vitro</i> screening cascade of a compound library against <i>S. mansoni</i> (inspired from [6]). B: Proposed <i>in vitro</i> screening cascade to ameliorate candidate selection, featuring an additional drug removal step on NTS.	3
1.3	PK/PD model (c.) combines the PK model (a.) describing “what the body does to the drug” (ADME) and the PD model (b.) defining “what the drug does to the body”; hence the effects.[13]	5
1.4	Circuitual model for a two-electrodes electrochemical cell.	8
2.1	Proposed microfluidic platform: outline and snapshot.	11
2.2	Statistical analysis, most frequent half-life values.	13
2.3	Stacked topology of microfluidic chip for automated drug wash-out. Substrate and components before assembly.	16
2.4	A) Mold for Flexdym™ soft lithography. B) Schematic view of molded and punched Flexdym™	17
2.5	Case of capillary stop. Unequal liquid levels for a single unit at the end of the transitory, large inter-unit variability.	20
2.6	Experimental setup for hydraulic resistance evaluation. Devices under test: PDMS chip and Flexdym chip.	22
2.7	Three frames of dummy PDMS chip flux monitoring. 12 μL/60 μL loading of amaranth water-based solution.	22
2.8	Outline diagram of the fluorescence assay with FITC-water based solutions. [29]	24
2.9	Detection of NTS parasite motility by the EIM platform. [1] A) Analysis unit and readout outline. B) The power of the signals acquired from motile and non-motile NTS parasites. The dotted line indicates the mean value of the signal power for motile (blue) and non-motile (red) NTS. The shaded areas show ±3 standard deviations. The power unit refers to 1×10^{-6} a.u. C) Frequency-response analysis of the EIM platform (100 mV AC voltage applied).	27
2.10	Simplified design space for ADC/DAC number of bits selection.	29

2.11	A) Design of the EIM platform PCB and analysis unit. [1] B) Outline of the electrical equivalent circuit of the experimental setup. C) Recorded impedance with the next-version platform, replacing the PCB and the analysis unit with a 3.3 k Ω resistor.	31
2.12	Measurement setup: TIA PCB (a), RedPitaya SoC (b), control PC (c). . .	32
2.13	Noise level measurements at different down-sampling frequencies and for signal re-sampling. Excitation signal: 200 mV _{pp} sinusoid at 488 kHz A) Noise level vs down-sampling frequency (shorting input/output RedPitaya). B) Noise level vs re-sampling frequency, selecting data at regular intervals (DUT-resistor). The down-sampling frequency of the original signal is 35 kHz (red point in the graph).	33
3.1	Comparison between hydraulic resistance estimations, from the fit of experimental data, and expected values from Comsol [®] simulations. . . .	35
3.2	Outline diagram of the assay for concentration measurements featuring FITC-based water solutions and mean fluorescent intensity profile over time in mixing units. [37] [29]	37
3.3	Mean fluorescent intensity profile over time of positive controls. [37]	38
3.4	Mean fluorescent intensity profile over time in mixing units without normalization with respect to positive controls. [37]	38
3.5	Outline diagram of the OXE assay with NTS suspensions. [29]	39
3.6	Variations in motility index of the vehicle-control sample (exposed to 0.5 %v/v DMSO) and of NTS exposed to 4 different OXE concentrations [1].	39
3.7	Time-lapse images of NTS showed qualitative movement patterns of NTS exposed to 25 μ M OXE (Flexdym chip).	40
3.8	Time-lapse images of NTS showing qualitative movement patterns of NTS exposed to 25 μ M OXE (PDMS chip).	40
3.9	Time-lapse images of NTS showed qualitative movement patterns of NTS exposed to decaying 12.5 μ M to 4.2 μ M OXE (Flexdym chip).	41
3.10	Time-lapse images of NTS showing qualitative movement patterns of NTS in negative control (Flexdym chip).	41
3.11	Time-lapse images of NTS showed qualitative movement patterns of NTS exposed to 12.5 μ M OXE (Flexdym chip).	41
3.12	Temporal evolution of the IC ₅₀ values for oxethazaine as determined by using impedance-based detection. [1]	41
3.13	Comparison in signal fluctuations power between the two readout platforms.	42
3.14	Bright-field microscopy images of a few motile NTS*.	42
A.1	Poiseuille flow in a circular tube (inspired from [38]).	48
B.1	Cause for surface tension in a liquid-gas interface A) Molecule in the bulk: all bonds saturated B) Molecule close to the interface: lacking chemical bonds (dotted lines), increased chemical potential. [40]	51

B.2	Scheme for Young contact angle of a three-phase system: gas phase, flat solid surface, liquid droplet.	53
B.3	Outline diagram of cylindrical capillary: relation between capillary pressure and contact angle (edited from [40]).	53
C.1	Demodulation in a lock-in amplifier.	58
D.1	Simulink model: block diagram.	59
D.2	Outline of data processing: from ADC sampling to noise level.	60
D.3	Noise level as a function of the ADC/DAC number of bit. Down-sampling at 1 kHz.	63
D.4	Noise level as a function of the ADC/DAC number of bit. Down-sampling at 1 kHz and re-sampling at 31.25 Hz by discarding data.	64
D.5	Noise level as a function of the down-sampling frequency. Sampling frequency and ADC/DAC number of bits respectively 4 MHz and 14 bits.	64
E.1	Comsol [®] sub-model I: geometry.	66
E.2	Comsol [®] sub-model II: geometry.	71
E.3	Comsol [®] sub-model II: mesh.	71
E.4	Reservoir regions for local concentration profile extraction.	72
E.5	Exemplar concentration profiles for r_{res} , R_{hyd} and $l_{channel}$ respectively equal to 2.25 mm, 23.4 kg/mm ⁴ s and 11 mm.	72
E.6	Half-lives of concentration profiles vs hydraulic resistance at constant reservoir radius.	73
E.7	Half-lives of concentration profiles vs reservoir radius at constant hydraulic resistance.	73
F.1	Steps of SU-8 photolithography.	76
H.1	Schematic of the TinaTI [™] model.	81
H.2	A) Output noise spectrum. B) Trans-impedance gain as function of input frequency.	82

Chapter 1

Introduction

Reliable and efficient screening methods are required to discover novel drug candidate compounds. New candidates need to be identified to treat schistosomiasis infection, a neglected tropical disease [1]. The main focus of this work is schistosomiasis infection and *S. mansoni* drug screening. A brief introduction about the disease is provided, together with the description of the state-of-the-art screening cascade. Then, a new concept for improving the screening cascade and different methods of viability estimation, with a focus on electrochemical impedance spectroscopy (EIS), are presented.

1.1 Schistosomiasis overview

Schistosomiasis - also known as bilharzia - is a tropical disease caused by a group of parasitic worms called schistosomes. Six species of schistosomes infect humans: *S. haematobium*, affecting genital and urinary tracts, *S. mansoni*, *S. japonicum*,

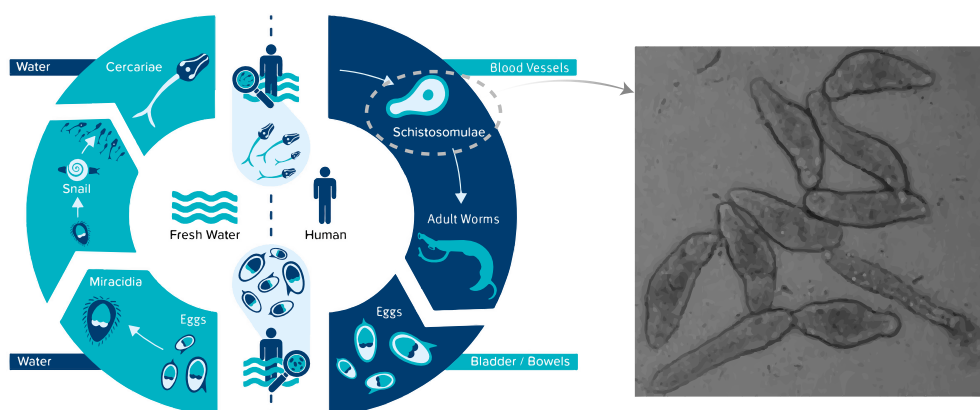


Figure 1.1. *S. mansoni* life cycle [2] and NTS representation.

S. mekongi, *S. guineensis* and *S. intercalatum*, affecting the intestinal tract.

Schistosomiasis infection is prevalent in tropical and subtropical areas due to the presence of water infested by cercariae, the schistosome form able to penetrate the human skin. Schistosomulae, i.e. the cercariae losing tails upon skin penetration, are the the first stage to infect human body. After infection, schistosomulae become adult over 5-7 weeks and reproduce. Adult schistosomes are not neutralized by the immune attack of the human body and thus are able to live for years inside the human host. The eggs, released by the female, cause the symptoms of the infection and progressively damage human organs. Part of the eggs is ejected in urine or faeces and can evolve into cercariae through snails infection [3]. The complete lifecycle is summarized in Fig. 1.1.

If left untreated, the infection gradually evolves to become a debilitating chronic disease, leading to anemia, malnutrition and undermined children growth. Blood in excretions, abdominal pain, diarrhoea and fibrosis of liver, intestines and/or bladder are other symptoms related to the type of schistosome. In the worst cases schistosomiasis infection lead to urogenital cancers and death. [4]

Today, according to conservative estimates, schistosomiasis affects around 230 million people worldwide, however a similar amount of people is expected to have residual morbidity after infection. Due to the transmission characteristics and to the countries considered endemic for the disease, schistosomiasis is one of the neglected tropical diseases prioritized by the WHO [5]. Neglected tropical diseases (NTDs) are a class of diseases affecting the poorer section of world's population, which historically got less attention with respect to other diseases. Preventive chemotherapy is a strategy commonly adopted in tropical areas to reduce morbidity of NTDs. The same applies for schistosomiasis since many mass drug administration campaigns were performed over the last decades. The improvement of water and sanitation together with behavioural modifications would be an effective way to reduce morbidity, nevertheless is an expensive approach. [3]

For over 40 years, praziquantel (PZQ) has been the only chemotherapeutic agent available for treatment against worm infection. Concerns have already been expressed due to the emergence of praziquantel drug resistance along with the fact that the current anthelmintic drug discovery pipeline is alarmingly unproductive. [1] Since preventive chemotherapy persists as the main tool against schistosomiasis, new antischistosomal drugs are needed to provide an alternative to PZQ.

1.2 *S. mansoni* drug screening

Drug discovery may be a long and onerous task, further complicated in the field of NTDs due to the limited amount of investments. Conversely, compound libraries of pharmaceutical and academic organizations offer a potential source for identification of candidate therapeutics. Screening of compound libraries is the antischistosomal drug discovery strategy at the base of this work and comes with numerous advantage with respect to new drug development. The first may result in successful and cost-effective repurposing of drugs, as with antimalarials for schistosomiasis. Drug repurposing consists in the development of new indications from existing, failed or abandoned drugs. Multiple benefits naturally come from repurposing, e.g. the possibility to profit from pre-clinical data, saving time and costs, making more informed decisions on hit-to-lead identification and ultimately decreasing the time necessary to bring a drug to market. [6] Drug repurposing is commonly adopted for schistosomiasis, due the advantages brought by the strategy.

The recovery of adult schistosomes is a laborious process, requiring intensive use of laboratory animals to let the schistosomes mature. Additionally, a few groups are able to recover an high number of schistosomes from the host and to perform long term screening. Since a large number of drugs must be tested, throughput needs to be enhanced. A first step towards higher throughput screening has been taken in the last years, since the more abundant *S. mansoni* newly transformed schistosomulae (NTS) were used for an initial hit selection prior to testing on adult parasites. [7]

Within this framework, considering [6], the state-of-the-art screening cascade for drug testing can be outlined as in Fig. 1.2A. NTS are better suited for initial selection among a large number of compounds, therefore the larvae are an important test

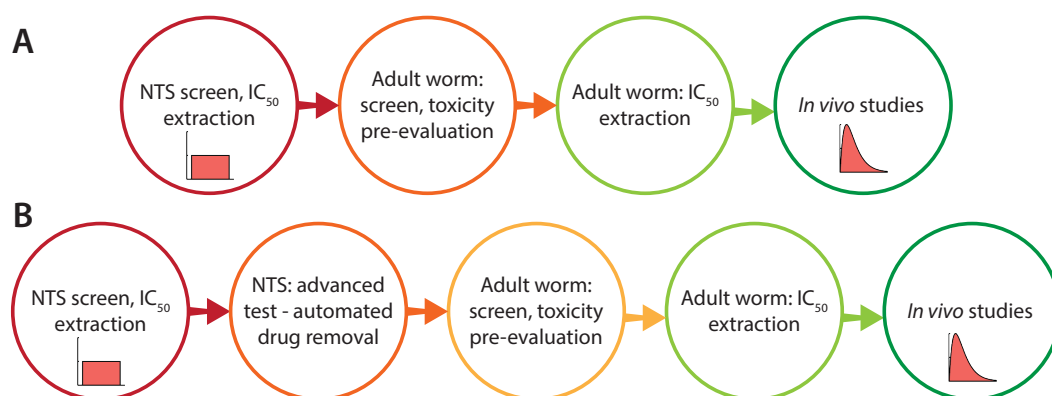


Figure 1.2. A: State-of-the-art *in vitro* screening cascade of a compound library against *S. mansoni* (inspired from [6]). B: Proposed *in vitro* screening cascade to ameliorate candidate selection, featuring an additional drug removal step on NTS.

subject, despite potential differences in effectiveness with respect to adult worms¹. In the related assays, the viability is assessed microscopically by a skilled operator who scores the morphology and motility of NTS. Hits on the larval stage are characterized as compounds which lead to a decrease in viability score under a predetermined cut-off threshold in the of the assay (typ. 24 h to 72 h). Ultimately, the activity of the selected compounds is often related to the IC₅₀ at a reference time point. The IC₅₀ is the half-maximal inhibitory concentration, an operational term dependent on the assay conditions but crucial in drug testing as relatable, in principle, to the binding kinetics [8]. Nevertheless, the IC₅₀ of a candidate compound is not the only parameter to be considered, as evidenced by numerous failures in the *in vitro* to *in vivo* translation. Additional parameters for compound optimization should be thought-through, for instance the *in vitro* dissociative half-life [9], the drug pharmacokinetics and the related pharmacodynamic profile (insights in Sec. 1.3).

A limitation of the standard NTS screening lies in the fact that a constant concentration is applied. Since scoring is performed during exposure, any observed decrease in viability might not be safely identified as permanent. A more exhaustive study may include viability evaluation upon removal of the drug. Actually, manual drug wash-out is a valuable tool in specific studies on *S. mansoni*. Sharma et al. [10] used a drug wash-out for the assessment of long-term therapeutic action of PZQ-based molecular probes, in order to get some insights about PZQ mechanism of action. Similarly, McCusker et al. [11] implemented a wash-out step to get insights about the mechanism of action. Starting from the confirmed activity of meclonazepam (MCLZ), the authors wanted to test other compounds of the same class (benzodiazepines) to identify the parasite target and eventually find better alternatives to MCLZ, lacking MCLZ side-effects. Both studies featured incubation of *S. mansoni* adult worms in presence of different concentrations of each compound,² an initial visual scoring, then a wash-out step and successive scoring after incubation in drug-free medium. Still, the decision of the time points for end-point scoring after wash-out was different, 7 d for the first study, 3 h and 24 h for the second one. Through manual wash-out in both cases compound selection was improved, e.g in [11] scoring after wash-out led to the conclusion that only a subgroup of the tested compounds causes extensive ultrastructural damage whereas other benzodiazepines only cause transient paralysis.

Even in studies on other stages of *S. mansoni* life cycle drug-wash out is valuable. For instance, Kamel et al. [12] assessed long-term therapeutic action of primaquine on juvenile (3-week-old) and adult (7-week-old) *S. mansoni* worms through visual scoring first at the end of a 24 h-assay, then after overnight incubation in drug-free

¹Praziquantel, the drug of choice for mass drug treatment campaigns, is less effective on NTS and juvenile worms. The converse is also true, as some compounds may result active on NTS but not on adult worms, e.g. screening in [6].

²Overnight in [10], 14 h-long in [11].

medium.

Due to the advantages brought by the wash-out procedure, if increased throughput could be provided, a drug wash-out assay early in the screening cascade would be advantageous for better *in vitro* selection prior to *in vivo* testing, as outlined in Fig. 1.2B. For instance, an hit confirmed by the new assay would have good reliability, high activity, fast and permanent action. As a consequence, a lower number of drugs may be selected for screening on adult schistosomes and in-vivo testing, limiting the use of laboratory animals for drug discovery. A candidate chip for wash-out implementation should be able to provide a physiologically relevant concentration profile, so as to ensure the improvement in hit selection.

1.3 Pharmacokinetics and Pharmacodynamics

Drug concentration close to the target site and activity *in vivo* is affected by different factors. Indeed, after drug administration, the compound is gradually removed through a series of metabolic processes. The drug-body interaction as a whole is the object of pharmacokinetic (PK) studies and can be subdivided into four different

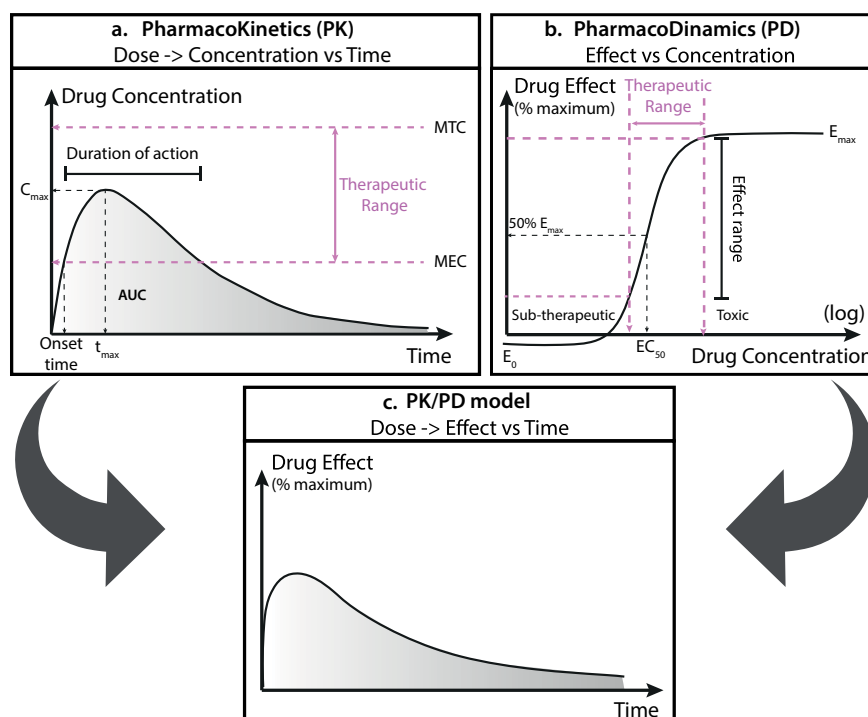


Figure 1.3. PK/PD model (c.) combines the PK model (a.) describing “what the body does to the drug” (ADME) and the PD model (b.) defining “what the drug does to the body”; hence the effects.[13]

phases, referred to as **ADME**: **A**bsorption, **D**istribution, **M**etabolism and **E**xcretion of the drugs. PK studies are performed to adequately dose the drug in a safe way, limiting side effects and enhancing therapeutic ones. [13] This applies especially to the selected application, where an excellent safety profile is required, as the optimal drug for treatment of schistosomiasis would be widely used in preventive chemotherapy campaigns, mainly targeted towards children. [6] Finally, the drug reaches the correspondent target and the related pharmacodynamic (PD) model describes the relation between concentration at the target and effect.

A comprehensive approach to derivation of drug effects would consider the full PK/PD process. Upon reversible drug effect, the PK/PD model may be represented as in Fig. 1.3. From the PD point of view, for explanatory purposes, the Hill equation is considered, although a more refined model may be required in practice. From the PK point of view, the concentration profile should be taken into account. Depending on the form of administration, the maximum exposure may be reached at a different time point and then the concentration decays due to drug elimination, up to the point that the drug is no longer effective. Various parameters are used to describe this curve in diverse compartments of the body, since drug distribution and decay are inhomogeneous across diverse regions. Among the others, half-life ($t_{1/2}$) is a typical measure of the residence time of the drug in the human body. By definition, $t_{1/2}$ is the time required for plasma concentration to decline by one-half when elimination is first order.³ [14] Most considerations on drug PK are relevant for specific studies downstream of hit selection and are mainly related to dosage of drugs with proved efficacy. Nonetheless, by being a description of the concentration decay, the half-life of candidate compounds could be a valuable information for a model concentration profile. In fact, a statistical analysis was performed in this work, so as to select a range of common half-lives to consider for the microfluidic chip design (insights in Sec. 2.2).

1.4 Strategies for viability assessment of *S. mansoni*

As stated in Sec. 1.2, a large number of drugs must be tested for drug repurposing, which therefore requires the use of medium- or high-throughput assays for screening. An ideal assay would be efficient and cost-effective, however the current gold standard involves worm phenotypic evaluation through operator-based microscopy, limited in throughput, labor-intensive, and subjective. Nonetheless, the introduction of NTS

³Easily determined by definition for mono-exponential decay of drug concentration. For multi-exponential pattern a reference value may be either related to an effective elimination rate, including clearance of a major part of the dose, or to the elimination rate in the terminal part of decay.[14] Usually independent of body size, preferably obtained from intravenous studies.

for initial hit selection posed the basis for the development of automated and higher-throughput systems. [1]

Similarly to the gold standard for adult worms, the principal way to evaluate NTS viability is through visual scoring by a skilled operator. With reference to the standard method, image-based automated microscopy was proposed to assess NTS viability through computer-based scoring of morphology and motility. [15] Bayesian categorization was successfully applied for scoring down to 10 schistosomulae, enabling hit selection and identification of relations between larvae structure and drug activity upon exposure. Nevertheless, due to the limited parallelization and to the high computational burden the proposed system was conceived for end-point viability evaluation, rather than continuous monitoring.

Isothermal microcalorimetry (IMC) is a label-free technique which allows to accurately and continuously monitor biological samples by measuring the related heat flux. The technique was proposed as an alternative approach to evaluate schistosomes viability, since heat produced by the larvae under exposure was proved to be a valuable indicator of drug activity. [16] IMC allowed to identify the onset of drug action and, due to the high sensitivity, even small changes in viability could be quantified. However, the high number of parasites required for well (c.a. 400 NTS) and the high cost of equipment with respect to the standard microscopy setup are the main downsides of the proposed method, impeding IMC usage for high throughput screening.

EIS was identified as a workable tool for real time monitoring of drug effects on adult worms, with the impedance-based xCelligence system for viability detection in a 96-well plate format, and can be extended to NTS [17]. Electrical impedance spectroscopy (EIS) readout is a non-invasive and label-free technique for inspecting the dielectric properties of a sample and their variations within a specific frequency range.⁴ Modena et al. [17], in a microfluidic chip for NTS monitoring, demonstrated that confinement in small sensing regions and the use of electrodes with dimensions comparable to the ones of NTS enable the possibility to assess the viability of the larvae through motility measurements. As a continuation, a drug screening system which can automatically measure NTS viability and continuously assess dose-response effects, was recently developed by Ravaynia et al. [1]. The proposed electrical-impedance microwell (EIM) platform included 32 analysis units able to perform analysis at constant drug concentration, even in absence of sub-millimetric physical confinement, by further optimizing the electrode size and spacing. This improvement enabled the use of a large medium reservoir and hence favoured long-term culturing of the parasites without an excessive impact on viability. However, the produced platform was still not ideal as an additional coating step was required during chip fabrication and impedance measurements were performed through a HF2-LI impedance spectroscope (Zurich Instruments AG, Zurich, Switzerland), increasing the overall cost. The proposed prototype can be made more cost-effective by replacing the used demodulator

⁴Insights in [Sec. 1.5](#)

block, with a price tag of around 25 000 €, with a low-cost dedicated one for the specific application, as will be done in this thesis. Actually, since this thesis work was performed in the Bio Engineering Laboratory of ETH Zurich, the aforementioned EIM platform is the main reference of this work and EIS was chosen to investigate NTS viability.

1.5 EIS and NTS monitoring

Electrochemical impedance spectroscopy consists in the investigation of the electrical impedance of a solid/liquid interface, which can provide information on bulk properties and surface phenomena. The processes and factors of concern are the ones that affect the charge transport across the electrolyte or between the latter and the electrodes. The study of these phenomena must comprehend the whole system, i.e. a collection of interfaces named electrochemical cell. An electrochemical cell is commonly constituted by 2 or 3 electrodes separated by at least one electrolyte phase. Generally a small-amplitude AC voltage is either applied or measured between two electrodes and, depending on the frequency range, the potential difference may fall almost entirely near the interfaces, alongside the so-called Helmholtz planes, or across the electrolyte. By appropriately choosing the electrode and the working frequency, changes in the electrolyte impedance can be monitored.

The commonly used equivalent circuit for modeling the electrode interface is the Randles circuit, composed by an electrolyte solution resistance in series with the parallel between a charge-transfer resistance and a double-layer capacitance, due to the ions located in the Helmholtz planes. In a more refined model, a Constant Phase Element (CPE) would replace the double layer capacitance. [18] Since the interest of this work are bulk changes of solution conductivity due to NTS, an electrode with minor charge transfer effects is appropriate. A perfectly polarizable electrode, i.e. an electrode with almost no charge transfer with the electrolyte (e.g. platinum), better fits the needs.

The two-electrode sensor configuration is the simplest one and a more complex experimental setup is not required for this application. The complete equivalent circuit is depicted in Fig. 1.4. The electrode where the AC voltage is applied takes the name of Reference Electrode (RE), conversely the electrode from which the corresponding

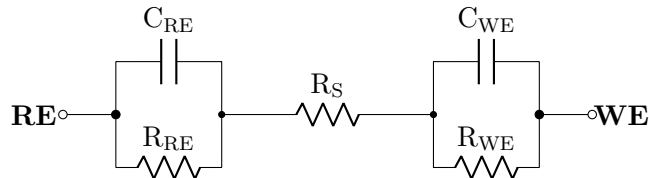


Figure 1.4. Circuit model for a two-electrodes electrochemical cell.

current is measured is named Working Electrode (WE).

For the specific application, the medium resistance behaviour over time is examined. The presence of the NTS on top of the electrodes, covering large part of the sensing area⁵, works as a hindrance for the electric field lines. Therefore, any movement of the larvae results in redistribution of the field lines, which is detectable through an appropriate readout system that constantly monitors the medium resistance. The signal consists on the relative variations of impedance caused by the slow contraction/extension (~ 1 -2 movements for second) of the NTS, rather than on the average impedance value. Being the impedance variation quite low (less than 1 %) signal demodulation stands as the most effective tool to reliably measure the weak signal related to the larvae, hence the need of a demodulator block (see [Sec. 2.8](#)).

⁵25 nL in [1] with an adequate sizing of the electrode, first, and of the well, second.

1.6 Aim of the project

The need for high-throughput drug testing on NTS and the advantages of a wash-out step in the screening cascade are outlined in [Sec. 1.2](#). The commitment to improve the EIS platform for continuous NTS monitoring of Ravaynia et al. [1] is stated in [Sec. 1.4](#). Starting from these demands, the aims of this project [19] are the:



- Development of a tubing-free microfluidic chip for antischistosomal drug-washing tests:
 - Physiologically relevant drug removal
 - Simple advection/diffusion mixing (no pump or tilting systems)
 - Reliable dose-response curve extraction
- Development of a low-cost dedicated mini-demodulator block for parallelized HTS

The development of the microfluidic chip for automated drug wash-out is driven by the intention of simplifying the wash-out practice by addressing some limitations of the manual one. The effectiveness insights tied with manual wash-out come with a cost, the drawbacks of an operator-based procedure. The manual wash-out practice is tedious to perform and requires an intrinsically higher experimental time, in terms of pipetting and scoring steps, thus reducing the throughput and increasing the complexity of the assay. Furthermore, the time points for end-point evaluation must be selected carefully a priori. On the other hand, a new controlled and simple platform featuring EIS readout may overcome the limitations of the manual procedure through a physiologically relevant dilution and continuous impedance-based evaluation, drastically diminishing the operator efforts. However, the platform should be transparent to allow visual scoring so as to verify the accordance between the standard evaluation method and EIS viability scoring. As a result, throughput may be increased and any onset of larvae recovery may be rapidly visible. Nonetheless, the devised platform fundamentally features a partial dilution, rather than a complete wash-out, as a design choice to keep the device as simple as possible. To accelerate the adoption process, the simplicity in the interaction of the end-user with the new technology should not be overlooked [20]. Ultimately, a suitable for drug dilution on NTS needs to be determined. Since the expected outcome of an assay with the developed chip is an improvement in candidate selection prior to *in vivo* testing, pharmacokinetic data could be a valuable support for chip design.

Chapter 2

Materials and Methods

This chapter contains all the aspects related to design, fabrication and measurement procedures. At first, a suitable experimental design was devised, striving for simplicity and physiological relevance. Then, starting from a statistical analysis of PK data from a library of potential candidates, the design requirements of the microfluidic chip were extracted. Subsequently, predictive Comsol[®] simulations were carried out to determine the profiles of volumetric flow rate and drug concentration. After devising the chip design, a suitable fabrication protocol was developed, overcoming some major fabrication issues. Experimental setups were prepared for prior validation of the chip, i.e. confirmation of concentration and flow rate profiles, and to run an entry-level assay with *S. mansoni* larvae. Finally, the design and the validation setup of the new prototype for EIS readout are provided.

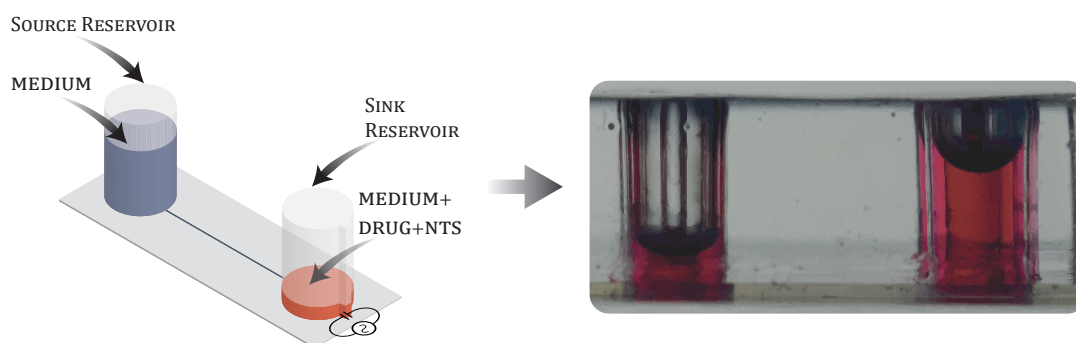


Figure 2.1. Proposed microfluidic platform: outline and snapshot.

2.1 Experimental design

The concept behind the proposed chip for mixing is gradual dilution by advection of medium across a narrow channel. A design simple, but able to preserve physiological relevance, was conceived to meet the objective. As depicted in [Fig. 2.1](#), the design features two cylindrical reservoirs with equal radius connected by a micro-metric channel. The reservoir with an additional trapezoidal feature is addressed as sink reservoir and is loaded with an NTS suspension, specifically a medium-based solution of the tested drug. The opposite reservoir, termed source reservoir, is formerly loaded with an higher volume of medium.

Therefore, at the start of the assay there is a difference between the piezometric heads of the two reservoirs. Being the reservoirs close-to-identical, as a first approximation no difference in capillary pressure is expected, therefore an horizontal piezometric head line between the two reservoirs is established asymptotically. Starting from the assumptions in [Annex A.1](#), a gravity-driven flux and hence mixing profile can be achieved with the chip, depending on the channel (hydraulic resistance), and on the reservoirs (radius and volume misproportions). Comsol[®] simulations are complemented to assess accurately the value of the hydraulic resistance and the concentration profile (see [Sec. 2.3](#)). Considering the viability readout, the chip should be ultimately provided with a pair of electrodes, analogously to the EIM platform of Ravaynia et al. [\[1\]](#).

2.2 Statistical analysis of small compound half-life

To guide the design of the drug-washing platform, a statistical analysis of PK data from a library of potential candidates was performed. The Pandemic Response Box, assembled for screening against infective and neglected diseases, was selected for this aim. The Pandemic Response Box is a collection of 400 antibacterial, antifungal and antiviral compounds, either already marketed or in various phases of drug discovery or development [\[21\]](#). Specifically, the half-lives of 107 compounds were taken into account to extract a range of most frequent values. Not all compounds could be part of the analysis due to the absence of in vivo pharmacokinetic studies for the excluded drugs. Moreover, literature estimates usually vary over a wide range, and there is consensus over pharmacokinetic values only for a limited number of drugs [\[14\]](#). The half-life values were taken from literature and from the DrugBank database [\[22\]](#). Further information about the sources is in [Annex G](#). The reported values span over a wide range of timescales, with few being either below 1 h or above 48 h and a close-to-normal distribution of their logarithms.

[Fig. 2.2](#) represents the distribution of these values, grouped into 16 bins under the Freedman–Diaconis rule, and a skewed-normal fit, preferred over the normal fit. The

criteria for selecting the first was the lower Akaike Information Criterion (AIC)¹, 229 for the skewed-normal and 233 for the normal distribution. After a visual inspection, the skewed-normal also appeared to be better able to represent the noticeable deviation between the median and the average value. For the following parts, any close-to-exponential decay halving at a suitable time was considered a physiologically relevant dilution. To extract a physiologically relevant timescale for drug dilution the 51 % most frequent drug were included (corresponding to 40 % of the total). Therefore half-lives in the 2.5 h to 13.1 h range were selected for the concentration profile in the chip to be designed.

¹A parameter for model selection among different statistical models, considering the number of fit parameters and the probability of seeing the data that are actually collected given a particular model (i.e. likelihood). [23] By definition: $AIC = -2L + 2k$, where k is the number of fit parameters and L is the logarithm of the likelihood for the fit. A low AIC , i.e. as close as possible to zero, the minimum value, is an index of good model selection.

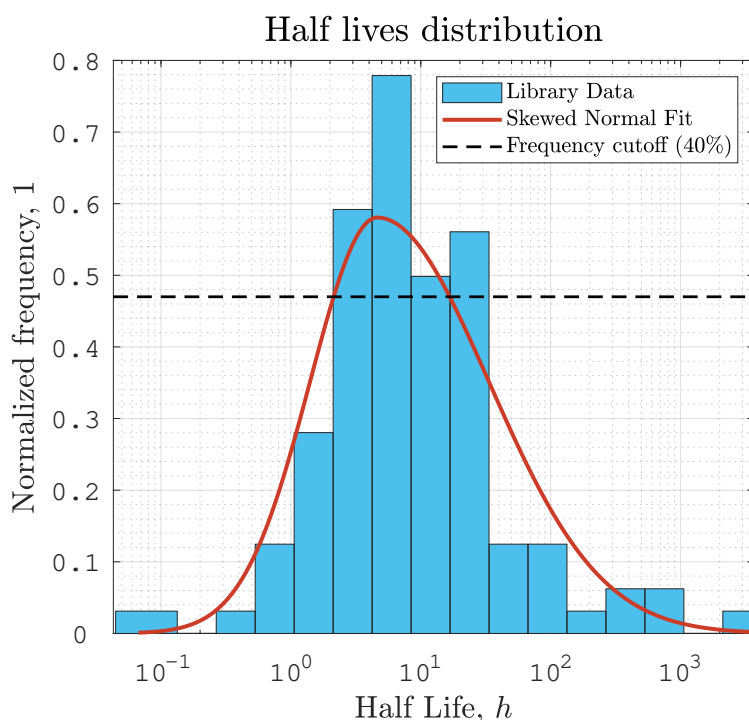


Figure 2.2. Statistical analysis, most frequent half-life values.

2.3 Comsol simulations

The proposed chip is constituted by two reservoirs connected by a narrow channel. The object of the simulations is to determine drug diffusion and advection in the reservoirs and in the channel.

Initially, some consideration were made about diffusion and advection of medium across the channel. Prior calculations showed that diffusion across the channel is largely negligible within 24 h (see [Annex E](#)). Therefore, diffusion was neglected for the following analysis.

Afterwards, advection of medium was characterized. The flux profile over time may be analytically derived and follows [Eq. 2.1](#), as derived in [Annex E](#).

$$Q(t) = \frac{g\rho_{mdm}}{R_{hyd}} \cdot \frac{V_{tot} - 2V_{drug}}{\pi r_{res}^2} \cdot \exp\left(-\frac{t}{\tau_{adv}}\right) \quad \text{with} \quad \tau_{adv} = \frac{R_{hyd}}{2g\rho_{mdm}} \cdot \pi r_{res}^2 \quad (2.1)$$

$$\Delta h(t) = h_{source}(t) - h_{sink}(t) = \frac{V_{tot} - 2V_{drug}}{\pi r_{res}^2} \cdot \exp\left(-\frac{t}{\tau_{adv}}\right) \quad (2.2)$$

In [Eq. 2.1](#), Q is the flow rate, g is the gravity constant, ρ_{mdm} is the density of the medium, R_{hyd} is the hydraulic resistance of the channel, r_{res} is the radius of the reservoirs, V_{tot} is the overall volume of medium, V_{drug} is the volume of medium with a non-zero uniform initial drug concentration, τ_{adv} is the time constant of advection decay. The decay of the flux depends on the hydraulic resistance of the channel and on the narrowness of the reservoirs. The principal method to tune the flux and the concentration profile is by changing the dimensions of the channel. Three different combination of channel parameters, featuring different channel length, were objects of further analysis. In [Tab. 2.1](#) the hydraulic resistance values from an ad-hoc Comsol[®] model are reported. Once the flux profile is established, the average normalized concentration follows [Eq. 2.3](#).

$$c_{broad}(t) = \frac{2V_{drug}}{V_{tot} - \pi r_{res}^2 \Delta h(t)} \quad (2.3)$$

Table 2.1. *Geometrical parameters, hydraulic resistances and related half-lives*

Channel			Reservoirs	Hydraulic Resistance	Half-life	
Height	Width	Length	Radius	Comsol [®]	Broad	Local
		7 mm		15.1 kg/mm ⁴ s	2.2 h	3.4 h
50 μm	75 μm	9 mm	2.25 mm	19.2 kg/mm ⁴ s	2.9 h	4.1 h
		11 mm		23.4 kg/mm ⁴ s	3.8 h	5.0 h

The latter expression describes the broad mixing kinetics, intended as a spatial average over the whole sink reservoir. This information was refined by a final Comsol[®] model, characterizing the concentration over time in each point of the sink reservoir. Specifically, in some regions of the reservoirs advection still dominates over diffusion, i.e. closer to the channel outlet, however in other areas the two contribution are comparable. Actually, at the opposite end of the reservoir with respect to the channel, diffusion causes a delay of the local concentration profile with respect to the broad mixing kinetics. Since any undershoot in the applied concentration due to an excessive advection contribution must be avoided, this region, which features an even slower mixing kinetics, was appointed as the more suited area for the parasites.

[Tab. 2.1](#) includes information about the selected geometrical parameters, complemented by half-lives for both the broad mixing kinetics and concentration at the location of the parasites. Additional information are provided in [Annex E](#). The latter design parameters were used in the subsequent steps of chip fabrication.

2.4 Fabrication and workflow

Once the design parameters were determined, the actual topology of the chip was established. As debated in [Annex A](#), thermoplastic polymers are the materials of interest due to the reduced costs with respect to silicon and glass, the simplified manufacturing procedures and the wide range of available polymer materials. Rapid-prototyping techniques were preferred to facilitate the fabrication process, while still being able to fulfil the design requirements. Therefore, the final protocol includes using materials such as Polymethyl methacrylate (PMMA) and Flexdym[™]. Fabrication limitations for realizing the specific design with the chosen materials were determined and adaptations were carried out to be able to fabricate prototype devices.

2.4.1 Stacked Topology

The demand for rapid and simple prototyping, while preserving the necessary resolution, led to the choice of a stacked topology. The chip was realized by bonding 2 components over a supporting glass slide², as shown in [Fig. 2.3](#). The 1st component was made out of Flexdym[™], which features the channel and the base of the reservoirs. The 2nd component was made out of PMMA, which features the larger part of the reservoirs.

²Thermo Scientific[™] Microscope Slides. Material: Soda-lime glass

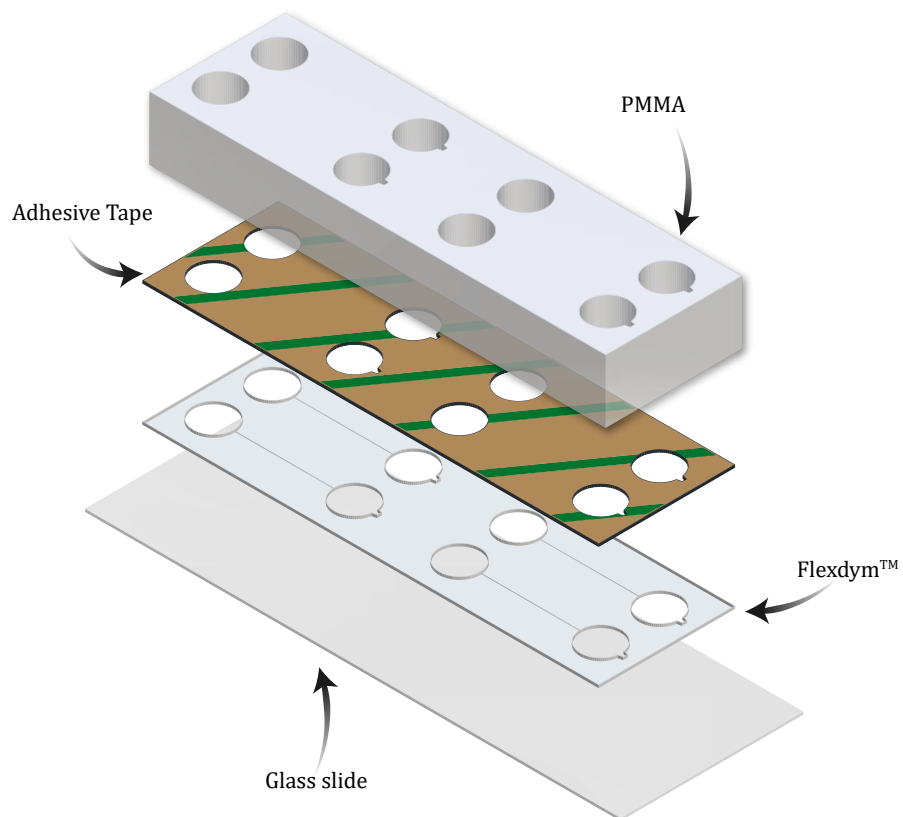


Figure 2.3. Stacked topology of microfluidic chip for automated drug wash-out. Substrate and components before assembly.

2.4.2 Components Patterning

Lower part: Flexdym Component

Flexdym™ is a thermoplastic polymer, chosen due to the appealing properties for microfluidic chip fabrication [24]:

- Certified bio-compatibility
- Negligible drug absorption
- Hydrophilic after plasma treatment
- Easy to fabricate

Flexdym® can easily be patterned through hot embossing. Therefore, starting from the theoretical design, a 2D foil mask was designed and ordered from Micro Lithography Services Ltd. In the simulated design of Sec. E, spatial constriction of the parasites was not addressed, therefore a slight modification, not included in the simulation since not relevant for the simulation purposes, was performed in the mask design. Specifically, a trapezoidal feature for collecting the larvae in the sink reservoir was added.

The fabricated mask was used to transfer the desired pattern into an SU-8 photoresist on the surface of a 4" silicon wafer through UV photo-lithography. The details about the procedure are contained in Sec. F. The procedure was repeated 4 times, leading to $48 \pm 2 \mu\text{m}$ ($50 \mu\text{m}$ mold primarily used). The silicon wafer with the SU-8 pattern was used as mold in the hot-embossing procedure. To prevent

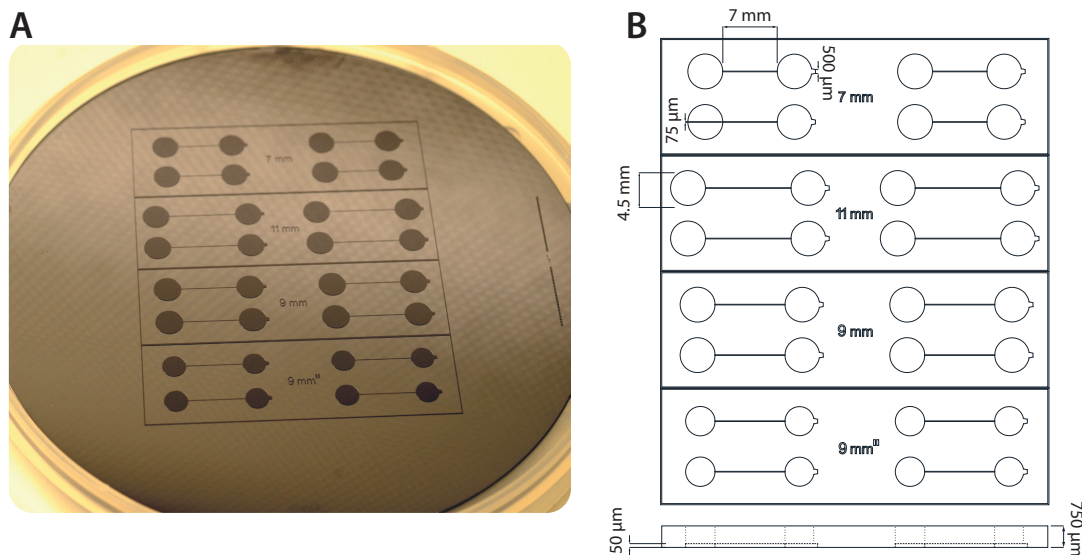


Figure 2.4. A) Mold for Flexdym™ soft lithography. B) Schematic view of molded and punched Flexdym™.

bonding to Flexdym, this mold was silanized (Low Pressure Chemical Vapour Deposition (LPCVD) with 3 μ L of Trichlorosilane, 4 h). The silanized mold was pressed into a 750 μ m-thick Flexdym sheet for 10 min at 5 psi.

The following steps were performed outside the clean-room, striving for preserving the cleanliness and hence the adhesiveness of the material through handling under laminar hood. Removal of small residues was performed using tape.³

The patterned sheet was diced into 4 components, each one featuring the base of the reservoirs and the channels of 4 mixing units, using a mechanical cutter. Finally, through-holes to the PMMA component, needed for the final assembly, were punched by using a metal hole punch plier. Since the puncher was positioned manually over the 50 μ m-thick reservoir footprints, the alignment to the chip features was strongly dependant on the accuracy of the operator. Nevertheless, the procedure is rapid and ensures that the adhesiveness of Flexdym is well preserved, as opposed to a laser cutting step. However, the current punching solution only provides circular hole due to the shape of the used tool⁴. The realization of the trapezoidal feature for trapping the parasites would require to use a custom-made tool, which was not used in this work and is postponed to future prototypes.

Upper part: PMMA Component

PMMA is a transparent, bio-compatible thermoplastic polymer, which can be readily patterned using CO₂ laser cutter, resulting in a clear cut with very few residues. Nevertheless, some residues of reflowed melted PMMA would appear close to the holes after cutting, which prevented the bonding of the Flexydim chip. To make the bottom surface more flat, a chloroform treatment was performed. The mentioned treatment consisted on a 3-minutes exposure of the component to gaseous chloroform.⁵ Formation of cracks was prevented by pre-heating the component (70 °C on hot-plate for 20 min) and chloroform exposure served as a sterilization step as well. Finally, once the chloroform was completely evaporated (70 °C on hot-plate for 10 min) a Biolipidure®-206 treatment [25] was performed to make the reservoirs hydrophilic.⁶ More details on the importance of surface treatment of the PMMA are reported in [Sec. 2.4.6](#). At last, the component is ready for the final assembly.

³3M™ Scotch® Magic™

⁴Available diameters 4 mm and 4.5 mm

⁵Chloroform poured into a glass Petri dish (volume dependent on dish size, level of 5 mm), PMMA fixed onto the lid with Kapton tape. Gaseous chloroform saturates the chamber once the lid is positioned.

⁶The component was temporally sealed on one side with Kapton tape. Then diluted Biolipidure®-206 (1:5 v/v into 50% ethanol sol.) was pipetted up to the brim of the reservoirs, left for 5 minutes, then removed. A second pipetting step was performed after 0.5 h to 1 h. Procedure as a courtesy from the authors of [25].

2.4.3 Assembly

The Flexdym component was bonded on the patterned side to a microscope glass slide. This bonding step was a thermally assisted adhesive bonding performed at 80 °C on an hot-plate overnight. On the opposite side Flexdym was bonded to PMMA. Although the datasheet reports that thermal treatment should be sufficient to bond Flexdym™ and thermoplastic materials [24], 24 h on hot-plate at 80 °C were not enough to achieve acceptable bonding, resulting in delamination and leakage. Therefore, bonding was achieved by using a double-sided adhesive tape⁷ where the shape of the reservoirs was patterned through the use of a CO₂ laser cutter.⁸

Adhesive bonding is strongly affected by the contact area, therefore the chip footprint has to be large enough to avoid failures and the region close to the reservoir has to be reasonably flat to avoid leakage. On the other hand, adhesive bonding through double-sided tape takes short time and doesn't require any thermal treatment of the components, thus ensuring that the Biolipidure®-206 treatment is preserved to a large extent. A 30-s O₂ plasma treatment was also performed to render the channel hydrophilic and to facilitate sample loading.⁹

2.4.4 Alternative approach: PDMS Chips

PDMS is the standard choice for rapid fabrication of microfluidic chips. This polymer is biocompatible for NTS assays [1], cheap and easy to process, however is not suitable for drug testing due to the high ad/absorption of small hydrophobic molecules. Coating of PDMS might be a viable solution to the ad/absorption issue, however a surface modification protocol also able to ensure a sufficient hydrophilicity¹⁰ was not established in this work. Nonetheless, PDMS was used in the fabrication of dummy chips for validation of the volumetric flow rate profile and suitability test with *S. mansoni* larvae. The dummy chips were fabricated by casting PDMS¹¹ on the SU-8 mold from Sec. 2.4.2. Casting was performed by pouring mixed PDMS a 10:1 elastomer-curing agent ratio, degassing for 1 h and thermally curing at 80 °C for 3 h. Finally, a PDMS component c.a. 4 mm high was detached from the mold and bonded to a microscope slide glass, after a plasma-activation step. (30 s at 50 W, 4 sscm O₂). To have a more stable hydrophilicity of the two reservoirs a Biolipidure®-206 treatment was performed, as in Sec. 2.4.3.

⁷3M™ Adhesive Transfer Tape 467MP

⁸Universal Laser System VLS3.75 with Bofa fume exhaust system, operating with 3 bar compressed air

⁹As a precautionary measure, to keep the bonding area hydrophobic the exposed surface of Flexdym was covered with tape and small openings were made on the reservoirs.

¹⁰Channels hydrophilicity is required to easily perform the loading steps and bubbles in the reservoir should be removed the end-user.

¹¹Sylgard 184 silicone elastomer

2.4.5 Loading procedure

The fabrication protocol was effective in producing an operable chip with 4 mixing units, each one featuring one source and one sink reservoir, connected through a narrow channel. Any assay on the chip was carried out as follows:

1. Sequential loading of the 4 source reservoirs (typ. 100 μL) with pure medium, i.e. water-based solution for pre-testing assays, M199 for assays with *S. mansoni* larvae.
2. Sequential loading of the 4 sink reservoirs (typ. 20 μL) with water-based solution for pre-testing assays, M199-based solution of the chosen drug and parasites for assays with *S. mansoni* larvae. In the latter case, successive pipetting of 2 equal aliquots: M199-based drug solution twice as concentrated, M199 and larvae.

Depending on the purpose of the experiment, Amaranth-Red or FITC water-based solutions, Oxethazaine M199-based solution were used. Due to the smaller capacity of PDMS reservoirs, volumes were scaled down to 12 μL /60 μL in dummy PDMS chips. As a final note, an adhesive plastic film was attached on top of each chip and 0.7 mm holes were made at the center of each reservoir to increase the relative humidity.

2.4.6 Main challenge: capillary stop

Besides bonding, the main challenge related to chip fabrication was an observed capillary stop of the flux of medium. The first assays were carried out without Biolipidure®-206 coating of the PMMA. As can be seen in [Fig. 2.5](#), the capillary pinning prevented the re-equilibration of the solutions, even after long equilibration times.

The hypothesis of remarkable deviation of the hydraulic resistance between the theoretical design and the fabricated chip was soon rejected. Indeed, the stop of the flux had a non-repeatable fashion from unit to unit, i.e. discernible difference in asymptotic volumes, and from a microscope measurement of a slice of the chip



Figure 2.5. Case of capillary stop. Unequal liquid levels for a single unit at the end of the transitory, large inter-unit variability.

the observed channel height was in the $50 \pm 10 \mu\text{m}$ range.¹² Any value of the channel height in the mentioned range would not be enough to explain the observed patterns. Therefore a specific study was carried out to address the issue. The devices under test were chips fabricated with the protocol of [Sec. 2.4.1](#) to [2.4.3](#) and similar chips in PDMS, whose fabrication protocol is explained in [Sec. 2.4.4](#).

A broader study of the forces at work would include, besides the hydro-static pressures of sink and source reservoirs, the capillary pressures. Therefore the asymptotic difference of fluid heights would be described by [Eq. 2.4](#).

$$\rho_{mdm}g\Delta h_{asymptotic} = \Delta p_{cap} = p_{cap}^{sink} - p_{cap}^{source} = \frac{2\gamma_{air/water}}{r_{reservoirs}}(\cos(\theta_{source}) - \cos(\theta_{sink})) \quad (2.4)$$

In the latter, $\gamma_{air/water}$ is the surface tension between air and water, $r_{reservoirs}$ is the radius of the reservoirs, g is the gravity constant, ρ_{mdm} is the medium density, p_{cap} is a capillary pressure, Δh is the asymptotic difference of liquid levels between source and sink reservoirs and θ stands for the contact angle at the PMMA-vapour-liquid interface in any of the two reservoirs. An extended discussion about capillary pressures and contact angle is available in [Annex B](#).

The basic assumption behind [Sec. 2.3](#) was that $\Delta h_{asymptotic}$ would have to be equal to zero, due to the fact that the two reservoirs were made out of the same material. However, the outcome of the first experiments clearly suggested that the assumption of zero $\Delta h_{asymptotic}$ was wrong. The ensuing working theory, based on the experimental results, was developed. The Young contact angle, and hence the reservoir hydrophilicity, depends on the surface free energy of the solid/vapor interface. The surface free energy is influenced by the presence of a water adsorption film, affected by the history of formation of the interface (see [\[26\]](#) and [Annex B.4](#)). The soon-to-be dried surface of the source reservoir (more filled) is expected to have a thicker adsorption film with respect to the soon-to-be wet surface of the sink reservoir. As a result, a difference in hydrophilicity arises, causing a difference in capillary pressures and hence the capillary stop.

Additionally, whenever a temporary treatment to increase hydrophilicity is performed, i.e. plasma treatment, the change in hydrophilicity may be reversed over time due to hydrophobic recovery processes (see [Annex B.4](#)). The hydrophobic recovery processes may change whether the material is kept in dry or wet conditions (e.g. from tens of minutes in dry conditions to days in wet conditions for PDMS [\[27\]](#)). If the hydrophobic recovery dynamics is substantially different between the two reservoirs, the asymptotic difference in liquid levels is increased.

These behaviours may occur in several polymers, therefore by using another material a non-negligible stop may be still observed. Nevertheless, once the dependency

¹²Measured on chip lacking the PMMA component with light microscope, 10x magnification

in Eq. 2.4 is acknowledged, one can rewrite the first as in Eq. 2.5,

$$\frac{2\gamma_{air/water}}{r_{reservoirs}}(\cos(\theta_{source}) - \cos(\theta_{sink})) = \frac{4\gamma_{air/water}}{r_{reservoirs}} \cdot \sin\left(\theta_{sink} - \frac{\Delta\theta}{2}\right) \cdot \sin\left(\frac{\Delta\theta}{2}\right) \quad (2.5)$$

assuming $\Delta\theta = \theta_{sink} - \theta_{source}$. Therefore, regardless of the mismatch between the source and sink contact angles, Δp_{cap} can become negligible for θ_{dry} PMMA adequately low. Hence, by treating the surface of the PMMA with Biolipidure®-206, which ensure that the surfaces remains highly hydrophilic during the whole assay, the capillary stop is drastically reduced.

Finally, relative humidity also plays a role in affecting the equilibration of the liquid levels, as affects the adsorption layer thickness of the sink reservoir instead, reducing the difference in hydrophilicity between the two reservoirs. A small capillary stop was still observed when the chip was left out of incubator in a plastic Petri Dish sealed with Parafilm¹³, as opposed to an assay carried out inside the incubator.

2.5 Hydraulic resistance measurement setup

The first test on the fabricated chip was the comparison between the theoretical hydraulic resistance and the experimental one. To this end, both regular chips and dummy PDMS chips were used.

¹³Bemis Parafilm® M All-Purpose Laboratory Film

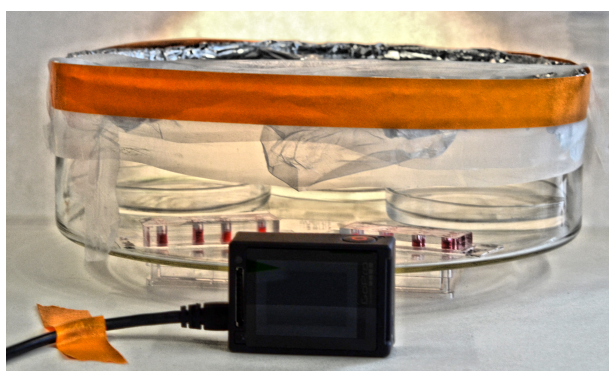


Figure 2.6. Experimental setup for hydraulic resistance evaluation. Devices under test: PDMS chip and Flexdym chip.

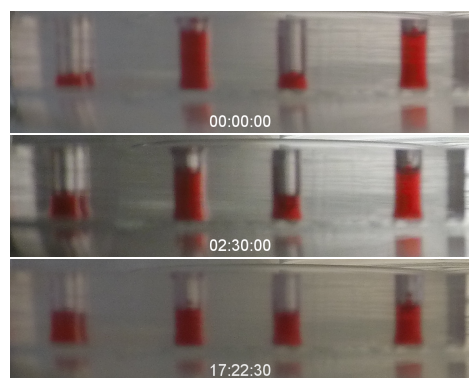


Figure 2.7. Three frames of dummy PDMS chip flux monitoring. 12 μ L/60 μ L loading of amaranth water-based solution.

To perform the flux-profile validation test both reservoirs were loaded with a 0.25 mg mL^{-1} amaranth-red solution.¹⁴ Two chips at a time were placed in a glass container, which was sealed with Parafilm and aluminium foil (see Fig. 2.6). Continuous imaging of the chip condition was performed at 2 photograms/min with a GoPro HERO7 Action Camera. For a significant number of photograms (8 logarithmically-spaced time points in the 0.5 h to 18 h range) the positions of the top and the bottom of the water meniscus were measured starting from the bottom of the associated reservoir (i.e. glass slide). The liquid level of the reservoirs was taken as the average number of pixel of the two foretold measures.¹⁵

The measured liquid level may be highly influenced by the measurement setup. Therefore, to reduce artefacts related to the position of the camera, the values of the sink and source heights for each chip were normalized with respect to the sum between the two. Finally, the normalized heights were used as data point for curve fitting to extract the experimental hydraulic resistance. To improve the fit accuracy, the levels of the sink and of the source were fitted contemporary. Since pre-testing was carried out outside of the incubator, the difference in hydrophilicity and thus in capillary pressures was enhanced by the low relative humidity. As a consequence, a small but appreciable capillary stop was present and an additional parameter was added to the fitting functions to include the asymptotic difference in liquid levels, as displayed in Eq. 2.6.

$$\begin{cases} h_{sink}^n(t) = \frac{1 - \Delta \mathbf{h}_{cap}}{2} + \left(\frac{1 + \Delta \mathbf{h}_{cap}}{2} - \mathbf{h}_{source}^n(\mathbf{0}) \right) \exp\left(-\frac{t}{\tau_{adv}}\right) \\ h_{source}^n(t) = \frac{1 + \Delta \mathbf{h}_{cap}}{2} - \left(\frac{1 + \Delta \mathbf{h}_{cap}}{2} - \mathbf{h}_{source}^n(\mathbf{0}) \right) \exp\left(-\frac{t}{\tau_{adv}}\right) \end{cases} \quad (2.6)$$

In the latter $h_{source}^n(t)$ and $h_{sink}^n(t)$ are the normalized liquid levels, the fit parameters are $\Delta \mathbf{h}_{cap}$, $\mathbf{h}_{sink}^n(\mathbf{0})$ and τ_{adv} . $\Delta \mathbf{h}_{cap}$ is the normalized capillary stop height, τ_{adv} is the advection time constant, $\mathbf{h}_{sink}^n(\mathbf{0})$ and $\mathbf{h}_{source}^n(\mathbf{0})$ are the apparent volume disproportions. For each mixing unit $\Delta \mathbf{h}_{cap}$ may vary due to inter-unit variability and camera position, $\mathbf{h}_{sink}^n(\mathbf{0})$ and $\mathbf{h}_{source}^n(\mathbf{0})$ may also vary due to the camera position. As shown in Eq. 2.1, τ_{adv} contains the information about the hydraulic resistance. Therefore, the value for the experimental hydraulic resistance may be extracted through the fit.

¹⁴Sigma Aldrich CORP A1016-100G Amaranth

¹⁵The meniscus in a quasi-static system takes the shape of a spherical cap, having the center of gravity roughly in the middle (negligible dependency with contact angle)

2.6 FITC Microscopy

The second test on the fabricated chip was performed to validate the simulations of the evolution of the concentration distribution for a small molecule compound initially loaded in one of the reservoirs. Fluorescein probes, including FITC, have the favorable spectral properties of visible absorption and emission wavelengths, high extinction coefficients, and reasonable quantum yields.[28] FITC is considered suitable since its molar mass (390 g mol^{-1}) resembles the one of most drugs such as Penicillin (330 g mol^{-1}) and Oxethazaine (470 g mol^{-1}), resulting in similar hydrodynamic diameters and, consequently, diffusion coefficients. Therefore assays for concentration testing were carried out through fluorescence imaging of FITC¹⁶ water-based solution. An inverted microscope (*NIKON Ti Eclipse*) with 10x 0.3NA objective, a CFI fluorescence light engine and a CCD camera were used. An advantage of using an inverted microscope combined with top illumination is the capability of effortlessly imaging any location from the bottom of the reservoirs. Furthermore, the surrounding atmosphere was maintained in an incubation box with gas mixing (*The Brick, Life Imaging Services*) and temperature (*The Cube, Life Imaging Services*) controllers, set at 95% humidity, 5% CO_2 and 37°C .

The control of microscope stage position, light intensity and shutter were done through an open-source software for microscope control (*Yoscope R2017*), which

¹⁶Sigma Aldrich CORP cat. no. F6377-100G Fluorescein sodium salt

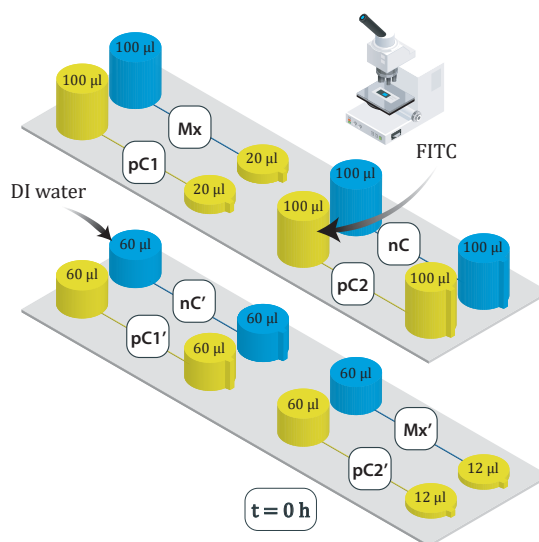


Figure 2.8. Outline diagram of the fluorescence assay with FITC-water based solutions. [29]

allows the user to set up automated controls [30]. Dissolved FITC was excited at 483 ± 25 nm and the emission was observed 524 ± 28 nm. Fluorescence images were acquired at the desired position every 30 min with an exposure time of 100 ms. Fluorescence intensity of each frame was analyzed with Image J [31], the extracted features were the average intensity of the image as a whole ($443 \mu\text{m} \times 443 \mu\text{m}$ area) and the standard deviation over the frame. The high-precision motorized focus z-stage allowed to easily focus at height of the channel and the depth of focus was expected to be around $10 \mu\text{m}$. However, as the FITC out of focus was also partially excited, a relevant signal contribution from the out-of-focus FITC could arise.

Furthermore, the relationship between signal intensity and FITC concentration is not linear: fluorophore-related phenomena such as self-quenching and photobleaching pose a challenge to accurate estimates. Self-quenching consists in a decrease in the quantum yield (and consequently of the fluorescence signal) due to non-fluorescent traps in the process of homo resonance energy transfer (RET). These traps act as a “sink” for the excited state energy. For fluorescein and other xantene-type dyes self-quenching is mostly due to resonance energy transfer between fluorescein molecules.[28] On the other hand, photobleaching consists in the fluorophore becoming unable to fluoresce for long periods (typically longer than the experiment time), as the molecule enters a dark state due to fluctuating local environments and transient interactions with other chemical species such as oxygen.[32]

To compensate the phenomenon of photobleaching, the lowest possible lamp intensity (2%) was set and to evaluate the contribute of out-of-focus FITC positive controls were included into the validation assay. Specifically pure DI-water and a 0.1 mg mL^{-1} water-based FITC solution were used in a variety of combinations and volumes to identify a relevant pattern. Both chips fabricated with the main fabrication protocol and dummy PDMS chips were used to this end. The loadings shown in Fig. 2.8 were performed, having lower volumes for dummy PDMS chips.

Being the feature initially designed for the parasites not extruded by punching and often gathering microbubbles, the imaged region was a $443 \mu\text{m} \times 443 \mu\text{m}$ square halfway between the botched feature and the center of the reservoir in the sink reservoir of each mixing unit.

2.7 NTS samples preparation

NTS suspensions were used in assays for drug testing. The larvae were obtained as in the followings. *S. mansoni* cercariae were harvested from infected intermediate host snails (*Biomphalaria glabrata*) and transformed into NTS using a state-of-the-art transformation method [33]. The resulting NTS suspension was adjusted to a concentration of $1 \text{ NTS } 2 \mu\text{L}^{-1}$, and the necessary volume was added to the sink reservoirs of each analysis unit to perform the measurements. Culture medium was

based on M199¹⁷ and optimized as by Ravaynia et Al. [1]. Incubation was performed at 37 °C, 95 % Relative Humidity (RH) and 5 % CO₂. For the drug wash-out experiments, the NTS were incubated in culture medium with diluted concentrations (12.5, 25 μM) of Oxethazaine¹⁸.

The NTS viability was qualitatively assessed through an inverted microscope (*NIKON Ti Eclipse*) with 4x 0.3 NA objective for 24 h every 30 min, after performing the loading of sink and source reservoirs. Preliminary evaluations of suitability of the fabricated chip were performed, as unambiguous pattern in larvae motility were pointed out by comparison rather than performing a state-of-the-art viability assessment, requiring visual scoring from a skilled operator.

2.8 Extracted specifications for the demodulator block

EIS viability measurement is a long-term target for the microfluidic chip in this work. As stated in [Sec. 1.6](#), the second part of this work is the development of a mini-demodulator block for parallelized high throughput screening.

Demodulation - also known as phase sensitive detection - is a valuable tool to recover signals within an overwhelming noise background. The technique consists on multiplying the signal by a sinusoidal reference, shifting the frequency spectrum by the frequency of the reference sinusoid. As a result of demodulation, the average value of the demodulated output corresponds to the frequency component of the input signal at the demodulation frequency (derivation in [Annex C](#)). A sufficiently high demodulation frequency allows to drastically reduce the impact of flicker noise¹⁹ and bandwidth reduction through an appropriate filter helps in lowering the electronics white noise²⁰. Both strategies are implemented in the EIM platform of Ravaynia et al. [1]. The resulting output voltage frequency response, recorded through the HF2-LI lock-in amplifier is shown in [Fig. 2.9C](#). Due to the flat response in the focused region, the selected working frequency was 500 kHz. Additionally there was no need to probe other frequencies since the dominant contribute at the aforementioned frequency is the targeted electrolyte solution resistance, which, according to our measurements, fell 2 kΩ to 4 kΩ range.

The NTS perform random movements, adding to the electrolyte solution resistance

¹⁷Thermo Fisher Scientific cat. no. 22340-020

¹⁸Sigma-Aldrich CORP cat. no. O5380-5G

¹⁹Term for noise phenomena regarding electronic devices having a $1/f$ behaviour in the frequency domain. These kind of phenomena are observed in different devices, although in many cases is not widely accepted mechanism.[34]

²⁰Term for electronic noise phenomena related to random processes, modeled as a constant contribution in the frequency domain.

a small contribution in the 1 Hz to 3 Hz frequency range. Applying a small AC voltage between the electrodes, the parasites modulate the output current, adding a frequency contribution in the neighborhood of the input signal frequency. On this basis, demodulation is performed at the frequency of the sinusoidal input voltage. Ultimately, the processed signal is a dimensionless signal, i.e. the high-pass-filtered demodulated output, normalized with respect to the DC component, as depicted in Fig. 2.9A. The viability indicator is then the signal power in the 1 Hz to 3 Hz range and typical values are reported in Fig. 2.9B. The recorded impedance variation, in terms of amplitude, is as low as 20 ppm, therefore high accuracy is required in data acquisition and processing.

Whenever possible, digital mixing in a demodulator block offers numerous advantages. Digital mixing involves early sampling of the signal and digital multiplication by a reference sine wave. Therefore, the mentioned technique features a perfect multiplication and minimizes the DC coupled electronics, needed with analog techniques, thus reducing output drift. [35] On the other hand a resolution sufficient to accommodate the signal and noise amplitudes is required. For the specific application the range will

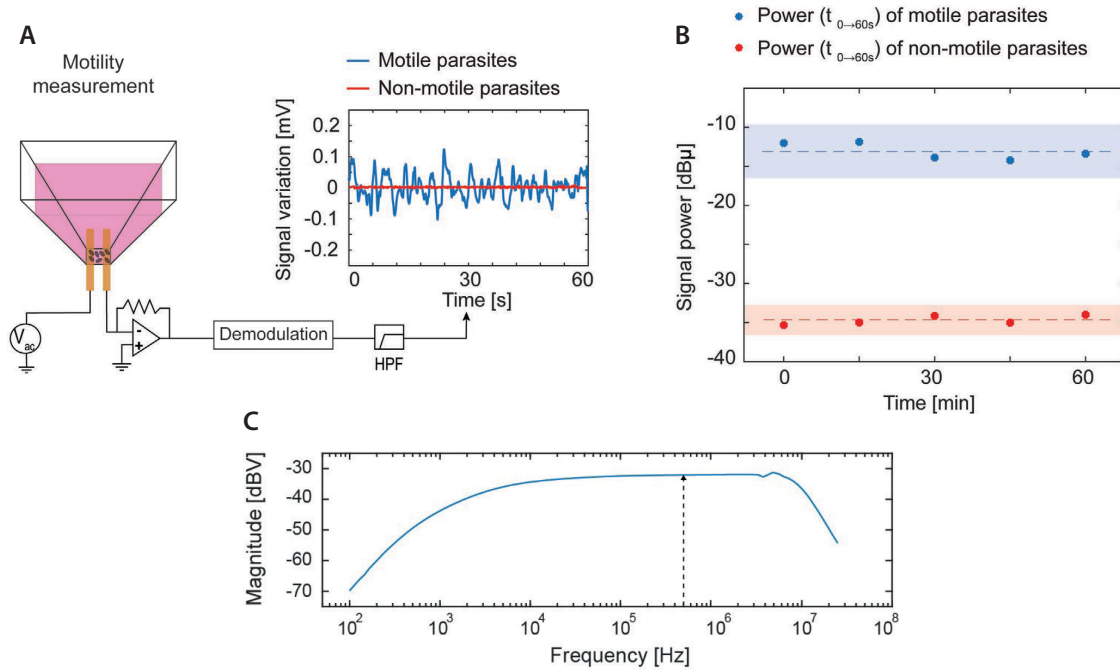


Figure 2.9. Detection of NTS parasite motility by the EIM platform. [1] A) Analysis unit and readout outline. B) The power of the signals acquired from motile and non-motile NTS parasites. The dotted line indicates the mean value of the signal power for motile (blue) and non-motile (red) NTS. The shaded areas show ± 3 standard deviations. The power unit refers to 1×10^{-6} a.u. C) Frequency-response analysis of the EIM platform (100 mV AC voltage applied).

be largely covered by the base value of the impedance, as the measured current is converted to voltage through a transimpedance amplifier (TIA), and the impedance changes should be larger than the least significant bit in the analog-to-digital conversion, which poses a strict requirement to the number of bits of the analog-to-digital converter (ADC). Furthermore, also the choice of the sampling frequency can provide lower noise, since digital down-sampling by sample averaging can then be exploited to reduce the white noise contribution of analog electronic components.

Due to the big amount of data which need to be acquired and processed, an optimal solution to effectively perform signal demodulation is a custom-built digital interface. An interface of this nature can be effectively created by using Field Programmable Gate Arrays (FPGAs). FPGAs are devices built around multiple configurable logic blocks, linked by programmable interconnections, which offer many advantages in terms of efficiency, capability of adaptation and short time-to-market. In this work, an FPGA will be used for signal acquisition.

2.9 Predictive simulations for demodulator components selection

The main sources of noise in the dedicated readout platform should be evaluated. Notably, the main sources are:

- ADC/DAC quantization noise;
- White noise and flicker noise of electronic components (e.g. TIA);
- Electrode related noise (e.g. due to evaporation).

Working in the Medium Frequency (MF) range, as the signal going through the electric equivalent circuit is a 500 kHz sinusoid (either modulated by the NTS movements or not) flicker noise may be neglected with respect to white noise as discussed in [Sec. 2.8](#). Still, the main limitation for an undersized system is expected to be ADC/DAC quantization noise, whereas in a workable system the electrode-related noise should be equal or higher to the other noise contributions.

A Simulink[®] model was created to assess the suitable number of bits for the ADC and DAC, as well as the related sampling frequency. Different combinations of parameters were considered in a simplified design space, featuring an equal number of bits for the ADC and the DAC, a TIA and a constant resistor as device under test (DUT). The full range of ADC and DAC was exploited ($2V_{pp}$ for the ADC, $200mV_{pp}$ for the DAC) and TIA noise, as well as quantization and quantization noise, were included in the model. In the simulation down-sampling at 1 kHz was performed by averaging the demodulated ADC data and 10s of signal recording were considered. The results are shown in [Fig 2.10](#). At each sampling frequency noise decreases exponentially by increasing the number of bits. Each point in the

graph corresponds to the first value below the $-41\text{ dB}\mu$ threshold.²¹ The identified working region is the one highlighted in light green. More insights on the simulations are provided in [Annex D](#). The choice of components was made accordingly in the followings ([Sec. 2.10](#)).

2.10 EIS measurement setup

Starting from the requirements in [Sec. 2.8](#) and [Sec. 2.9](#), a suitable readout system was built. The DUT was the impedance-based platform from Ravaynia et al. [1]. The submitted custom-made PCB of [1] enabled signal routing. Both input and output were given through SMA connectors and in the original experimental setup two SMA-BNC cables then connected this PCB to an external instrument (HF2LI, *Zurich Instruments*). The HF2LI operated as signal generator, producing a sinusoidal voltage at the working frequency for the PCB input, as TIA and as lock-in amplifier in processing the PCB output.

In this work the same system was used. However, the external lock-in instrument

²¹Being the power of non-motile parasites $-35\text{ dB}\mu$ in [1], a value four times lower for the noise power unrelated to the electrode can be reasonably selected as threshold.

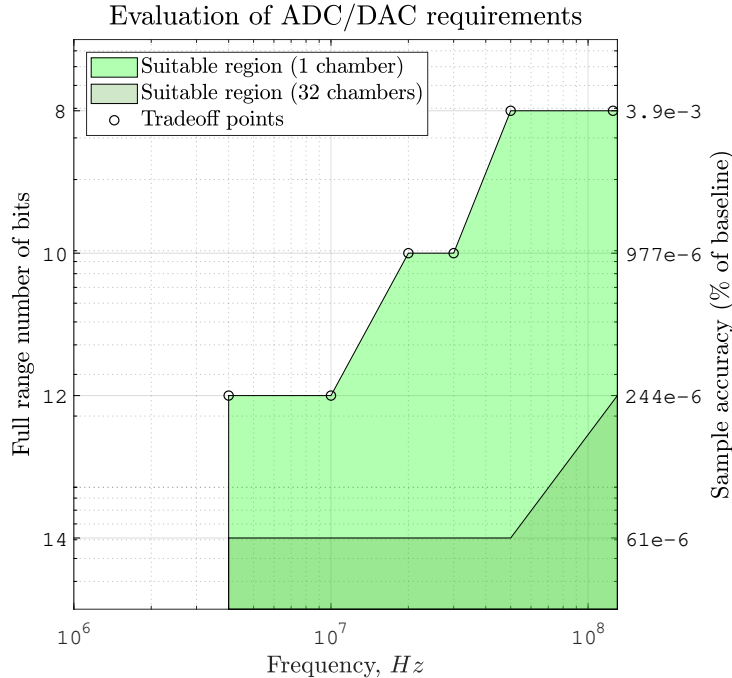


Figure 2.10. Simplified design space for ADC/DAC number of bits selection.

was replaced to realise an equally valid but cost-effective readout platform. Specifically, through a BNC-BNC cable, the signal coming from the output was given as input to a second PCB, featuring a wideband, low-noise TIA (OPA858 *Texas Instruments*). The added PCB is a modified version of the OPA858 EVM (*Texas Instruments*) where the amplifier is in transimpedance configuration with a feedback resistor of $30.10 \pm 0.03 \text{ k}\Omega$ between the output and the inverting input (inverting configuration). The output of the TIA was then guided through a BNC-BNC connector to a Basic Pitaya 125-14 SoC (*STEMlab*) for digitisation and processing. The used SoC, comprehends:

- 14 bits ADC (LTC2145-14, *Linear Technology*) and DAC (DAC1401D125, *NXP Semiconductors*), operated at 125 MS s^{-1} , compatible with [Sec. 2.9](#) design requirements;
- a programmable FPGA logic, set as a digital lock-in amplifier by using the RePLIA lock-in design by Stimpson et al. [36];
- a dual core processor, able to run a Linux operating system, thus convenient for communicating with an external computer where acquisition parameters are set and post-processing is performed.

Ultimately, the excitation signal was provided through a BNC-BNC connector by the Pitaya SoC using the built-in DAC and the RePLIA design. A schematic view of the prototype is shown in [Fig. 2.11B](#).

The exact value of transimpedance gain, by theory quite close to the value of the feedback resistor, was computed through a SPICE simulation on Tina TI™ (*Texas Instruments*). The circuit schematic and further information about this simulation are available in [Annex H](#). The extracted value of the transimpedance gain was $30.16 \text{ k}\Omega$.

Before using the designed instrument for *S. mansoni* drug testing, preliminary test were made by shorting the input and the output of the Red Pitaya. Then, the experimental setup of [Fig. 2.11B](#) was employed by replacing the DUT (PCB and analysis unit) with a $3.300 \pm 0.003 \text{ k}\Omega$ resistor. For the subsequent analysis, 1-minute recordings of the signal processed by the FPGA were used. The RePLIA design features two mixing blocks, respectively for the in-phase and quadrature components, followed by an IIR low-pass filter and a down-sampling block. The time constant of the low-pass filter is tunable and was chosen for each demodulation frequency accordingly to the optimization performed by Stimpson et al. [36]. The frequency of data transfer to the control PC, i.e. the sampling rate of the down-sampling block, is adjustable and a sampling rate of 35 kS s^{-1} was chosen (c.a. 14 kS s^{-1} and switching among multiple chambers in the EIM of Ravaynia et al. [1]). As for the parasite motility evaluation, the signal was zeroed and normalized by subtracting and dividing by the mean value. The power spectral density of the normalized and zeroed signal was computed and the power level obtained by integrating in the 1 Hz to 3 Hz range.

The RePLIA design features DDS units for excitation signal generation. The excitation signal was a $200 \text{ mV}_{\text{pp}}$ sinusoidal wave, therefore the full range of the DAC,

i.e. $2V_{p-p}$, was unexploited. For future improvements of the prototype, a voltage regulator could be added in series to take full advantage of the DAC number of bits. Finally, since noise levels were measured in the 1 Hz to 3 Hz window of the demodulated signal, spreading in frequency of the generated signal (a sinusoid at c.a. 500 kHz) may significantly affect the noise level in the frequency range of concern. Nevertheless, the DDS components of the design operate optimally taking as excitation and demodulation frequency a quotient between the FPGA clock frequency (125 MHz) and any power of two. By selecting the aforementioned frequencies the generated sinusoid is notably narrow in the frequency domain, resulting in optimal low-frequency noise.

Once the parameters of the experimental setup were set, the transfer function of the output voltage with respect to the input sinusoid was obtained through several measures over a large range of demodulation frequencies. The impedance extracted from the output voltage is shown in Fig. 2.11C. The results show good agreement between the expected impedance and the measured one in the passband (including the working frequency, c.a 500 kHz). To isolate the noise contribution of the PCB including

²²Single measure.

²³Average of 3 measures.

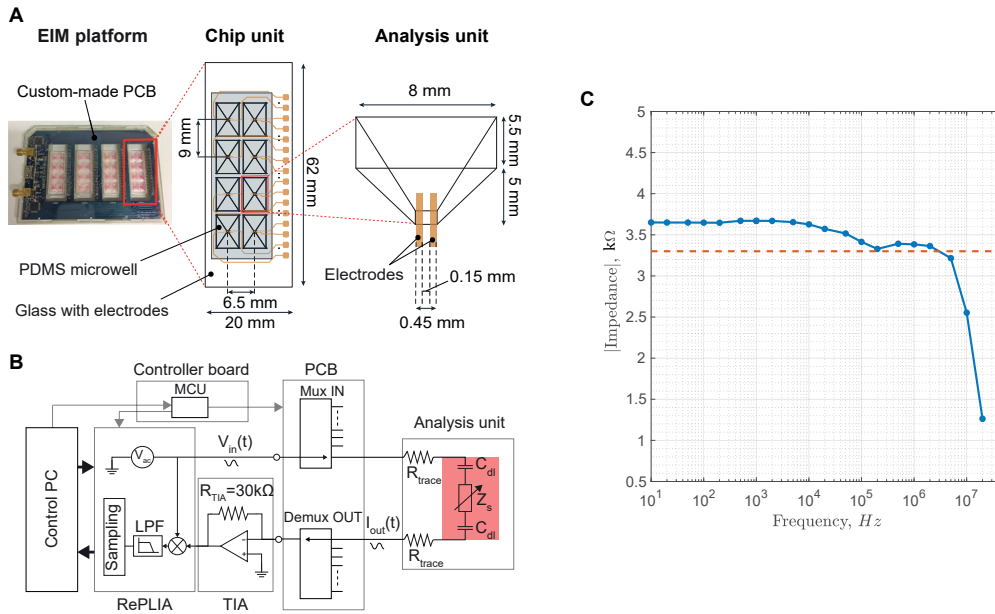


Figure 2.11. A) Design of the EIM platform PCB and analysis unit. [1] B) Outline of the electrical equivalent circuit of the experimental setup. C) Recorded impedance with the next-version platform, replacing the PCB and the analysis unit with a 3.3 k Ω resistor.

the chip, the noise level unrelated to the DUT was measured. The power of noise was measured for 4 frequencies in the passband, while either using the same setup as in Fig. 2.11B with the 30.1 k Ω resistor as DUT or using only the Red Pitaya, shorting input and output through a BNC-BNC connector. The related results are shown in Tab. 2.2. The noise values appear to be influenced by remaining low frequency components, observable in the power spectral density above the white noise level. The low frequency noise in the measured signal presumably comes from non-idealities in the generation of the excitation signal, as similar values are displayed in both measurement conditions.

Finally, the impact of down-sampling was investigated on the new platform. An initial test was performed by changing the down-sampling frequency of the RePLIA. The results are shown in Fig. 2.13A. The lowest down-sampling frequency features an higher noise level, which then decreases and stabilizes at c.a. -42 dB μ . Since in a NTS screening assay switching among chambers is performed, noise analysis for a single chamber is performed on a lower number of time points. Therefore, for a particular down-sampling frequency, the noise level was computed by re-sampling the signal, reducing the effective sampling frequency by discarding data. The results of this test are shown in Fig. 2.13B. The noise level remains virtually unchanged for a low number of discarded data, then increases as more data are thrown out.

Table 2.2. *Noise levels for simplified measurement setup.*

$f_{\text{demodulation}}$	Noise level ²² (DUT-resistor)	Noise level (shorting input/output Redpitaya) ²³	
		200 mV _{pp}	2 V _{pp}
30 kHz	-29.8 dB μ	-19.0 dB μ	-39.7 dB μ
122 kHz	-38.2 dB μ	-35.7 dB μ	-43.0 dB μ
488 kHz	-41.7 dB μ	-41.9 dB μ	-42.8 dB μ
1.95 MHz	-42.3 dB μ	-41.6 dB μ	-40.4 dB μ

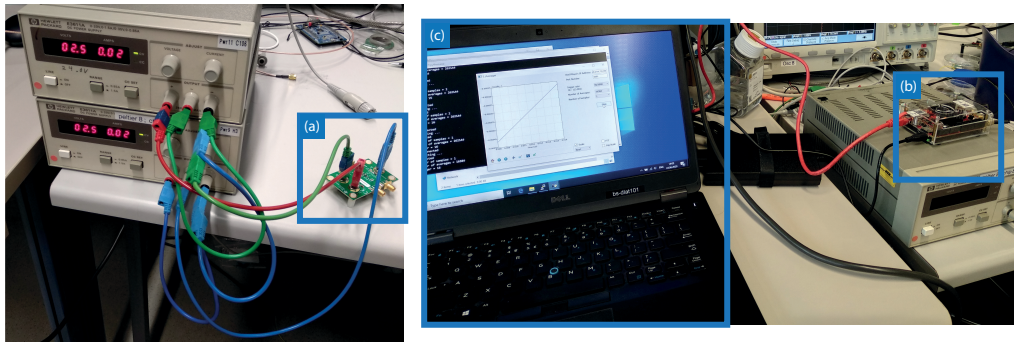


Figure 2.12. Measurement setup: TIA PCB (a), RedPitaya SoC (b), control PC (c).

Given the success of the initial tests, short electric recordings on *S. mansoni* larvae were carried out to estimate the level of signal fluctuations from the movements of the parasites. Both the new prototype and the last prototype, featuring an HF2 lock-in amplifier, were used in close succession. As a preliminary step for this set of measures impedance measurements without the NTS were performed to extract the transfer function of the complete system. To this end, 30 μL of medium were added into 4 wells that were used for characterization. Subsequently, 30 μL of NTS suspension were loaded in each well and impedance-based viability assessment was performed on all the chambers. The NTS suspension on chip was not homogeneous, resulting in diverse number of parasites among the chambers. Nevertheless, the variation of parasite number did not affect the result of the experiment since correlation between viability assessments with the two prototypes for the readout was achieved.

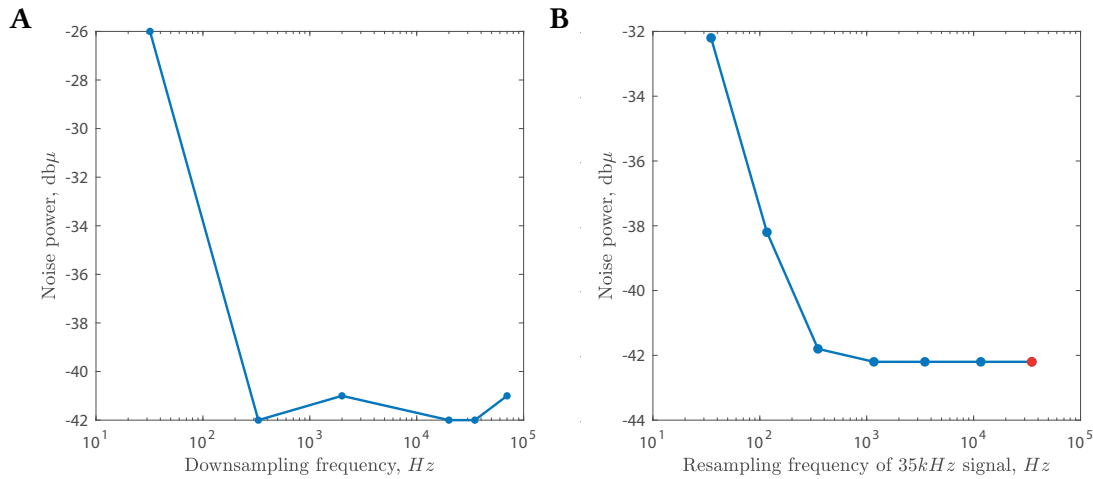


Figure 2.13. Noise level measurements at different down-sampling frequencies and for signal re-sampling. Excitation signal: 200 mV_{pp} sinusoid at 488 kHz A) Noise level vs down-sampling frequency (shorting input/output RedPitaya). B) Noise level vs re-sampling frequency, selecting data at regular intervals (DUT-resistor). The down-sampling frequency of the original signal is 35 kHz (red point in the graph).

Chapter 3

Results

In the followings, the results related to the chip and to the proposed platform for readout are presented. Starting from the chip validation, hydraulic resistance estimation and FITC concentration measurements are reported. Then the experimental results from the NTS assays are described. Finally, the outcome of viability estimation of *S. mansoni* parasites is reported.

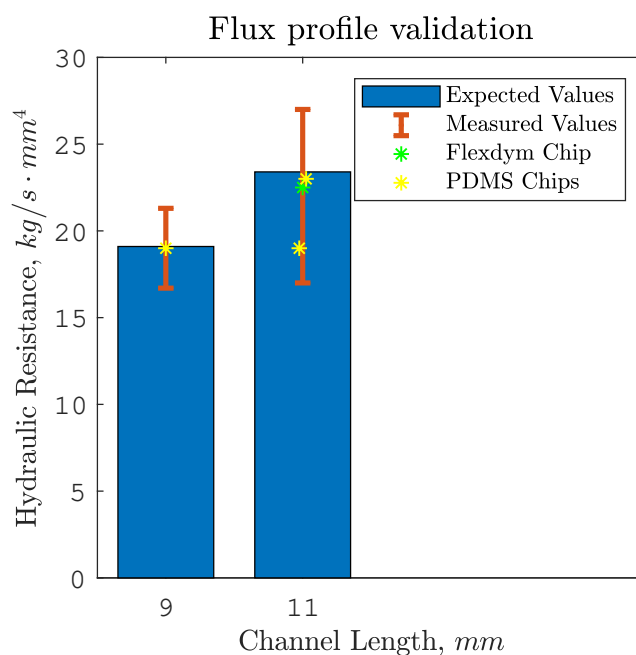


Figure 3.1. Comparison between hydraulic resistance estimations, from the fit of experimental data, and expected values from Comsol[®] simulations.

3.1 Hydraulic resistance estimation

Hydraulic resistance estimations were performed as outlined in [Sec. 2.5](#). Experimental and simulated hydraulic resistances are shown in [Fig. 3.1](#). Three units from PDMS and one Flexdym™ chips were included in this study, since the analysis was limited to the units where both the lower side of the reservoirs and the liquid meniscus were more distinguishable. The fit-related errors in hydraulic resistance estimation were computed for each unit and the quadratic mean of the errors is provided for each channel length, applying error propagation in equivalent units. The relative error at each time point for the liquid level, not included in the fit, was in the 5 – 15 % range. In practice, the absolute error on the liquid level was virtually constant (i.e. a few pixels), thus a lower relative error was obtained for the source and an higher one for the sink reservoirs. Nevertheless all reservoirs were included to have more points, globally resulting in an improved evaluation of all the fit parameters, as the asymptotic values.

The experimental and theoretical hydraulic resistances show good agreement, as can be seen in [Fig. 3.1](#), which demonstrates the validity of the simulated flow rate profile. Subsequently, also the average concentration in the sink reservoir is expected to follow [Eq. 2.3](#).

3.2 FITC concentration Measurements

FITC measurements were carried out as discussed in [Sec. 2.6](#). Two sets of measurements were performed. For each mixing unit, the z-focus was set to the height of the channel to minimize variability in signal intensity. For each chip, variability in z-focus among the 4 units was in the 40 – 100 μm range¹. The planar position was set by prioritizing regions with a homogeneous level of brightness² and inter-reservoirs changes in planar position may be considered an additional source of variability.

The results are shown in [Fig. 3.2](#). Out-of-focus fluorescence drastically affected the signal quality. Actually, the positive controls with varying volumes, i.e. condition pC1 and pC1', showed an increasing intensity over time. On the other hand, chips featuring dilution of FITC water-based solutions, i.e. condition Mx and Mx', exhibited slight decreases in concentration, less prominent than the counterparts. Therefore, the obtained data from condition Mx and Mx' were normalized with respect to the aforementioned positive controls, condition pC1 and pC1'. Finally, the negative controls, only loaded with DI-water, namely nC and nC' condition, were used only once, as repeatedly showed a small constant fluorescence background³. The resulting

¹Difference between extreme values of z-focus position among the mixing units.

²Selection of ROI in bright field microscopy before starting the assay.

³Pixel intensity around 100 Gy out of 32 000 Gy, having the lowest measured intensity of c.a.

background value was then subtracted from all measurements.

A second observation is the difference between the two sets of measurements. The asymptotic value of concentration in the sink reservoir is 33% of the initial one. On the upside, the same asymptotic values were not expected a priori for signal intensity, due to the unpredicted contribution of the out-of-focus FITC. Actually, for the first set of measurements the asymptotic value was indeed 33%, but for the other the asymptote was significantly higher (around 70%). Due to the limited amount of experiments on workable chips, such difference cannot be undoubtedly traced back to the conditions of the FITC solution, which was re-prepared in-between the set of experiments. Assuming the asymptotic variation attributable to the conditions of the FITC solution, the apparent kinetics of the second set of measurements is faster than the predicted one. Nevertheless, due to the high standard deviations at each time point, a reliable comparison between measured concentration profile and predicted one (see Eq. 2.3) is not an easy task and further investigations on fluorophore-related artifacts need to be done.

As a first observation, considering the intensity profile in condition pC1 and PC1', the out-of-focus contribution suggests that the final intensity profiles should be compared with the broad concentration profile, as the measured intensity is the result of a spatial average over a large volume. Therefore, any local concentration profile from the simulation cannot be compared with the results of this experiment. A validation of the local concentration profile would have been made either by using a confocal

3500 Gy (initial value of positive control for 2nd set of measures)

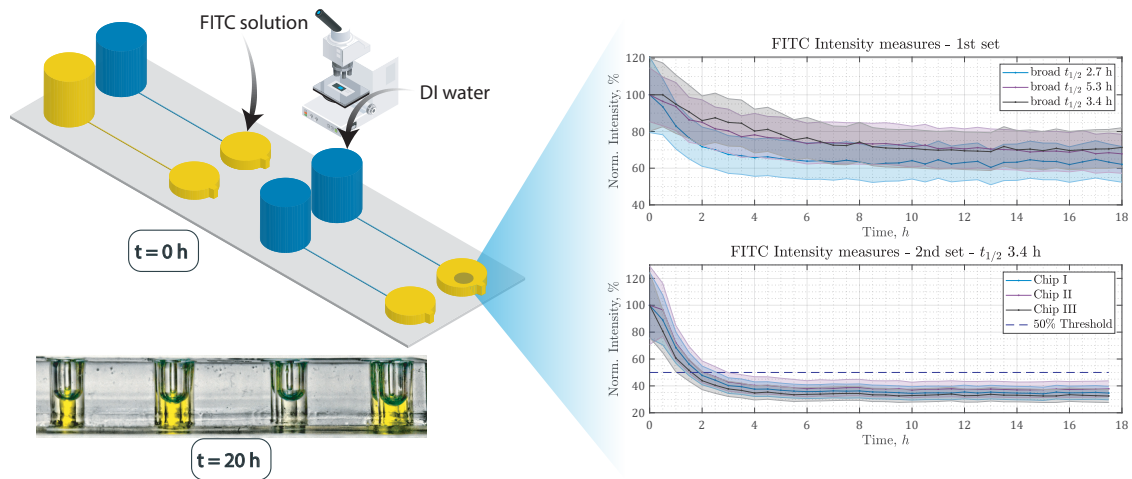


Figure 3.2. Outline diagram of the assay for concentration measurements featuring FITC-based water solutions and mean fluorescent intensity profile over time in mixing units. [37] [29]

microscope or by framing a sufficiently thin feature, which can be also wetted in a repeatable way (current issue).

Further analysis should be performed to ultimately validate the local concentration profile from the Comsol[®] simulation. However, as the chip at this point in development was reliable with regard to the volumetric flow rate profile (Sec. 3.1), preliminary analysis with NTS were performed, assuming the theoretical concentration profiles rationally valid.

3.3 Investigation of chip suitability for drug-washing assays on NTS

The final experiments with the fabricated chip were performed to assess the chip suitability for drug-washing assays on NTS. To this end, both PDMS chips (Sec. 2.4.4) and chips fabricated with the main protocol (Sec. 2.4.1 to 2.4.3) were used to highlight the difference between the two.

The rational motivation of the drug wash-out assay is to assess whether the drug of choice is a fast acting compound, able to rapidly cause permanent damage, or not. In fact, a candidate drug might only cause temporary inhibition of the NTS, e.g. by only reducing motility while present. Therefore, the motility of the parasites was observed for different concentration profiles in the sink reservoir, to monitor whether recovery, a sign of temporary inhibition, was present. Oxethazaine (OXE) was selected due to high lethality even at low concentrations. The reference motility and IC₅₀ graphs are reported in Fig. 3.6 and Fig. 3.12.

Only one set of experiments was performed, having different drug concentrations.

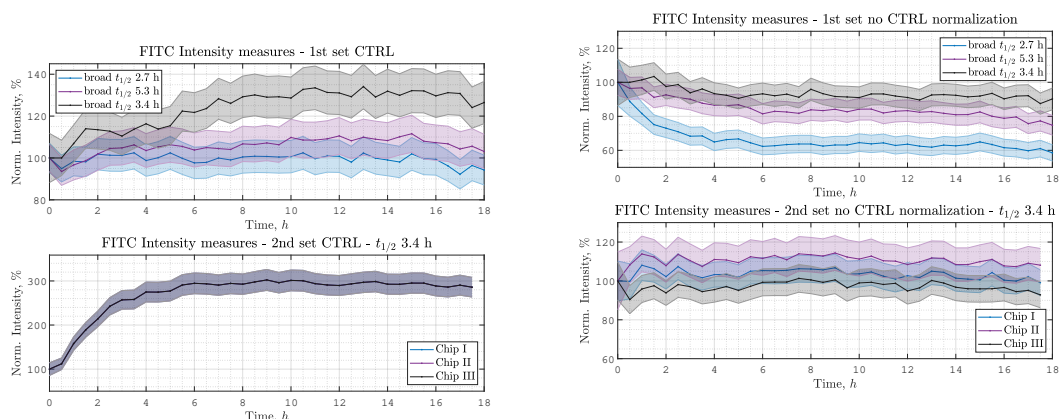


Figure 3.3. Mean fluorescent intensity profile over time of positive controls. [37]

Figure 3.4. Mean fluorescent intensity profile over time in mixing units without normalization with respect to positive controls. [37]

All conditions are shown in Fig. 3.5. Condition pC1 and pC1' served as major positive controls, having the highest initial concentration of drug ($25 \mu\text{M}$). In these conditions the concentration in the sink reservoir is constant and well above the $\text{IC}_{50}(0.5 \text{ h})$, c.a. $6 \mu\text{M}$, therefore NTS are expected to rapidly die within the first few hours of drug exposure. This wasn't the case for units from chip made out of PDMS. The NTS showed clear signs of recovery, with respect to the PMMA/Flexdym™ counterparts. The NTS in the PDMS chip distinctly appear to become more motile over time whereas the NTS in the plastic chip didn't show any sign of mobility. An initial remark, considering the discrepancy with respect to the Flexdym™ chip and to evolution of the motility index reported by Ravaynia et al. [1], is that oxethazaine concentration must have dropped during the experiment in PDMS chips. Furthermore the presence of recovery suggests that oxethazaine may cause temporary inhibition under short exposure, rather than permanent damage. To avoid PDMS absorption, a parylene coating was used to render the material more inert in previous experiments in the group. Uncoated PDMS is clearly not suitable for drug tests since the observed concentration drop is caused by drug absorption into the polymeric matrix. Parylene coating may be considered to solve this issue but having an hydrophobic coating for such a small channel would complicate the loading procedure (i.e. channel filling). On the other hand, Flexdym™, together with PMMA, appears to be a promising alternative.

Being uncoated PDMS unsuitable for drug wash-out assays, the focus was shifted entirely on Flexdym™ chips and eventual signs of recovery within those. Within the first hours, clear signs of recovery were observable in a mixing unit with initial drug concentration of $12.5 \mu\text{M}$, asymptotically decreasing to $4.2 \mu\text{M}$. The observed NTS

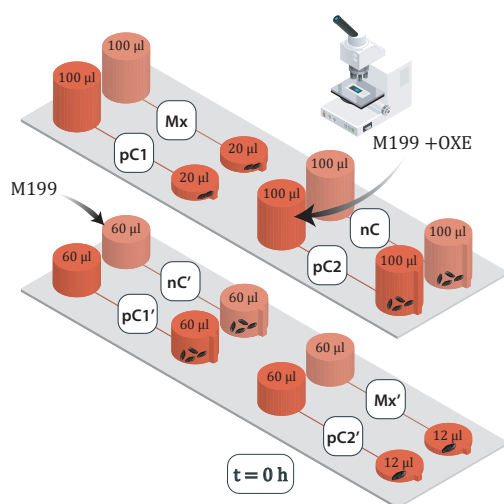


Figure 3.5. Outline diagram of the OXE assay with NTS suspensions. [29]

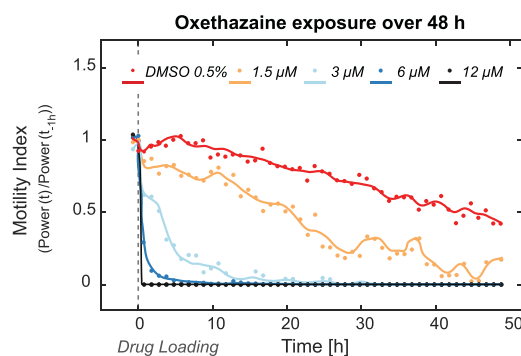


Figure 3.6. Variations in motility index of the vehicle-control sample (exposed to 0.5%v/v DMSO) and of NTS exposed to 4 different OXE concentrations [1].

were almost non-motile up to 3 h, then a distinguishable and widespread recovery in motility, becoming more and more evident over time, was observed from 4 h. The $IC_{50}(4\text{ h})$ from the reference article, extracted from constant concentration assays, is $2.4\ \mu\text{M}$, slightly below the asymptotic $4.2\ \mu\text{M}$, therefore poorly motile NTS would be expected. Nevertheless, any mixing unit needs to be referred to a relevant negative control to draw out substantial conclusions. Unfortunately most negative controls, except one, featured not very motile NTS, probably due to prior conditions of the larvae. The usable negative control showed clearly motile NTS in the first hours, but the parasites moved out of the ROI after 2.5 h, due to the high mobility and the lack of spatial constriction within the base of the reservoirs. However, due to the poor conditions of the negative control conditions (untreated parasites), the measurements need to be repeated. Nevertheless, the drug-exposed parasites show a clear recovery in motility after few hours, which highlights the importance of monitoring the response of the parasites to drug washout.

Another remark is that the positive control at constant drug concentration of $12.5\ \mu\text{M}$ showed slight signs of recovery, as depicted in Fig. 3.11. This result is not compatible with the reference article, being the expected $IC_{50}(4\text{ h})$ and $IC_{50}(8.5\text{ h})$ respectively $2.4\ \mu\text{M}$ and $2\ \mu\text{M}$. Possible explanations for the latter are errors in the experimental setup and long-term drug absorption by Flexdym™.

The results of this section provide useful tips for guiding next assays and to eventually ameliorate the prototype. The outlined experiment serves as a preliminary visual evaluation, appropriate at this stage of prototype development. The next step

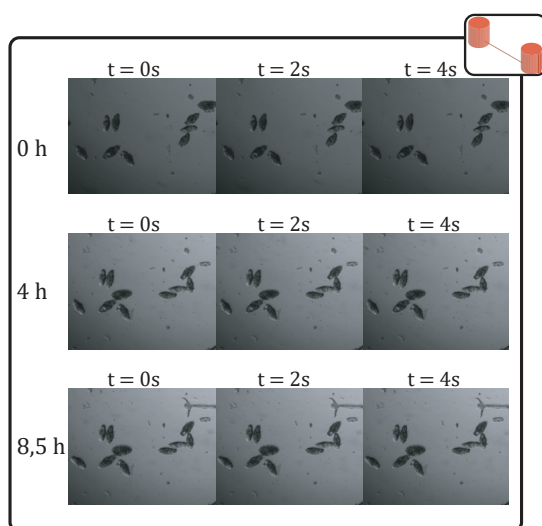


Figure 3.7. Time-lapse images of NTS showed qualitative movement patterns of NTS exposed to $25\ \mu\text{M}$ OXE (Flexdym chip).

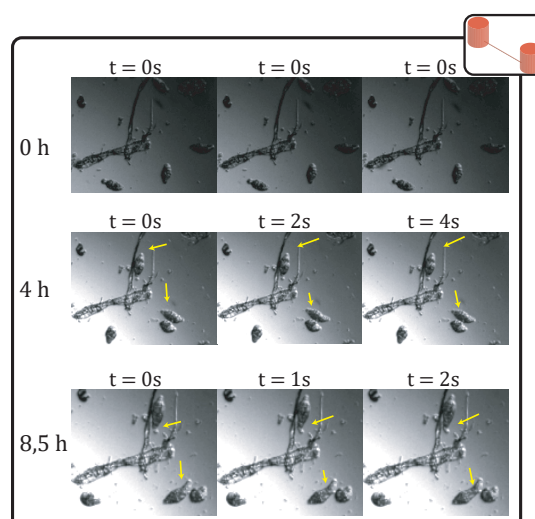


Figure 3.8. Time-lapse images of NTS showing qualitative movement patterns of NTS exposed to $25\ \mu\text{M}$ OXE (PDMS chip).

would be to improve the spatial constriction, possibly by tilting the chip stage, to add electrodes and to perform more accurate viability evaluations.

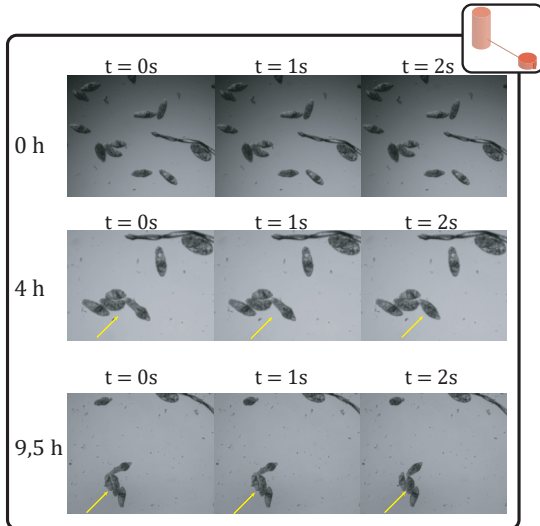


Figure 3.9. Time-lapse images of NTS showed qualitative movement patterns of NTS exposed to decaying $12.5 \mu\text{M}$ to $4.2 \mu\text{M}$ OXE (Flexdym chip).

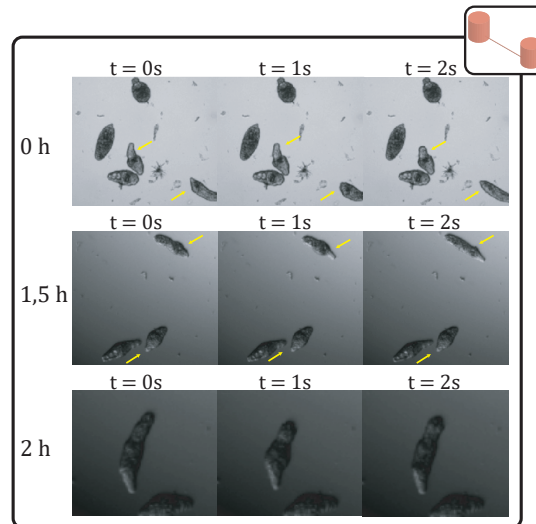


Figure 3.10. Time-lapse images of NTS showing qualitative movement patterns of NTS in negative control (Flexdym chip).

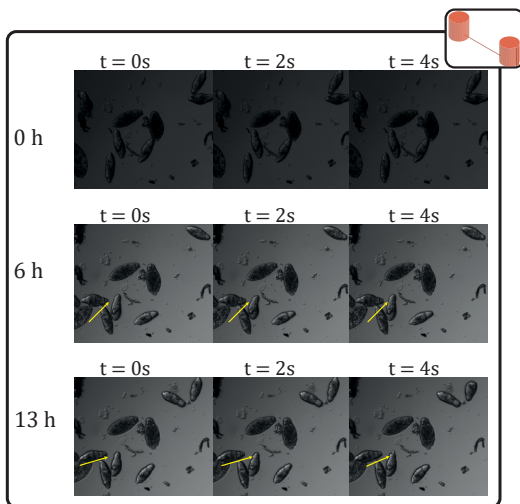


Figure 3.11. Time-lapse images of NTS showed qualitative movement patterns of NTS exposed to $12.5 \mu\text{M}$ OXE (Flexdym chip).

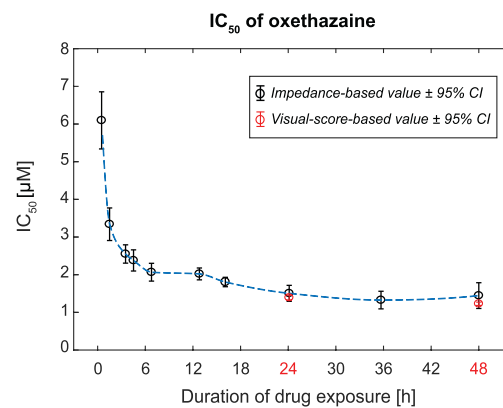


Figure 3.12. Temporal evolution of the IC_{50} values for oxethazaine as determined by using impedance-based detection. [1]

3.4 Impedance-based viability assessment of *S. mansoni* larvae

Focusing on the readout, a new readout platform was tested with NTS suspensions. As debated in Sec. 2.10, the custom made PCB of Ravaynia et. al. [1] was connected the HF2 lock-in amplifier, i.e. the standard instrument, and to the new prototype, i.e. TIA PCB wired to the Red Pitaya SoC. Noise estimation were performed on M199 medium only and on diverse NTS parasites suspensions. The results are shown in Tab. 3.13.

A strong accordance between the two readout platform is reported for the experimental conditions. Moreover, the power of signal fluctuations is reasonable since comparable with the values shown by Modena et al. [17]. Nevertheless, a high level of noise is reported with both readout platforms, with respect to the results of Ravaynia et al. [1], probably due to higher evaporation or electrode misalignment.

Figure 3.13. Comparison in signal fluctuations power between the two readout platforms.

	HF2	RePLIA
Medium	$-31.3 \text{ dB}\mu$	$-30 \pm 3 \text{ dB}\mu$
Larvae Group	$-10.9 \text{ dB}\mu$	$-11.0 \text{ dB}\mu$
Few Larvae	$-22.6 \text{ dB}\mu^*$	$-22.3 \text{ dB}\mu^*$
	$-22.7 \text{ dB}\mu$	$-23.8 \text{ dB}\mu$

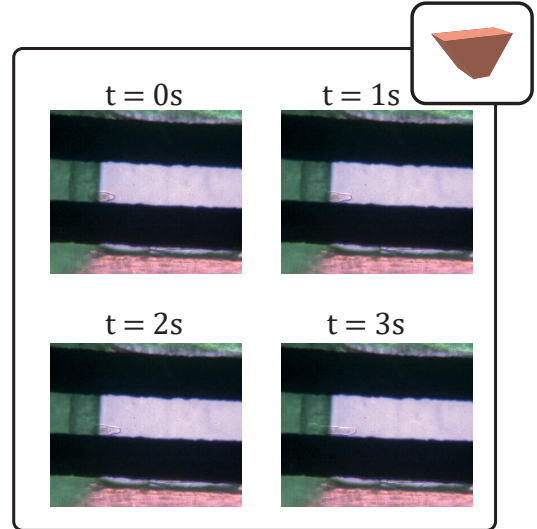


Figure 3.14. Bright-field microscopy images of a few motile NTS*.

Chapter 4

Discussion and conclusions

The first purpose of this work was to develop a tubing-free microfluidic chip for antischistosomal drug-washing tests. Great progresses were made in that direction, with the establishment of a fabrication protocol, using rapid prototyping techniques and promising materials, and the validation of the volumetric flow rate profile. Eventually, more efforts may be devoted to the experimental validation of the concentration profile by improving the setup for the detection of the fluorescence signal in the chip. Referring to the feasibility of the proposed chip for *S. mansoni* drug testing, some preliminary information was collected, e.g. details about NTS recovery by means of reduction of oxethazaine concentration. Ultimately, further analysis should be done, to completely rule out long-term drug absorption and to perform more accurate viability assessments, with an emphasis on negative control conditions (untreated parasites). Moreover, electrode implementation still needs to be done, together with a feasible spatial constriction of NTS, achievable with a good chance by tilting the chip.

The second purpose of this work was to build a low-cost dedicated mini demodulator block for viability measurements. The proposed demodulator seems to be ideal for this purpose, since the new component is significantly cheaper but presents similar noise performances under experimental conditions. However, data processing of impedance data at the software level needs to be improved to enable routine use of the platform.

The preliminary results, both on the development of the microfluidic chip and on the realization of a new readout instrument, demonstrate the feasibility of both improvements of the NTS assay and can serve as basis for future developments of an improved strategy for testing of candidate compounds on NTS.

Appendix A

Microfluidics

Microfluidic devices are any devices featuring fluid manipulation with components at the micro-scale, either actives (e.g. valves) or passive (e.g. micro-channels). Since the underlying assumption that the fluid may be considered as a continuous phase is still valid at the microscale, the physics for such devices, a branch of continuum mechanics, is the same as in the macro-world. Nevertheless, different effects are dominating, since osmotic forces, friction and surface forces (e.g. capillary forces) prevail. Furthermore, thermal diffusion is faster and liquid evaporation needs to be properly compensated due to the lower volumes. Actually, as the volume scales down, the exposed surface scale down more slowly, resulting in higher surface/volume ratio.

An handy parameter for describing the flow condition is the Reynolds's number. The Reynolds's number is a nondimensional parameter used to rewrite the Navier-Stokes equations, fundamentals of fluid mechanics, in a more convenient and generalized form. Nondimensionalization is strongly present in fluid-mechanics, since enables a compact description of the system, thus leading to generalization [38]. Specifically, the Reynolds number, defined in Eq. A.1, is the nondimensional parameter describing the type of flow.

$$Re = \frac{\rho U l}{\mu} \quad (\text{A.1})$$

In Eq. A.1 ρ is the fluid density, μ is the dynamic viscosity, U and l are respectively the characteristic velocity and length of the system of concern.¹ For $Re < 2000$ the flow is said to be laminar or viscous-dominated. The fluid appears to move in orderly sheets or lamina and for specified boundary conditions, a single flow is experimentally observed. Due to the dimension of the devices in microfluidics, a laminar flow, stable to perturbations, is always observed, enabling the possibility to have a fine control over microenvironment, valuable for numerous applications.

¹Geometrically relevant length, extracted by considering the development of the fluid flow, and related velocity.

In biological research, microfluidic devices carry important advantages, namely the reduction of sample volume, implying lower expenses for reagents and samples, the possibility to take advantage of phenomena such as capillarity, osmosis, electric double layer and the opportunity to integrate sensors (e.g. electrodes) and/or multiple functionalities on the chip. Furthermore the reduction in device size, parallel and fast processing result in high throughput, raising scalability for screening applications. [20]

A.1 Fundamentals

As specified in the introduction to this annex, the fluid is considered as a continuous matter. Therefore a fluid volume small with respect to the dimensions of the system of concern, but still containing a large number of molecules, can be considered for the following derivations. In fluid-mechanics, the Navier-Stokes equations describe the behaviour of a liquid phase and cannot be solved analytically, if not for specific cases. Therefore, whenever feasible, the fluid is assumed to be incompressible, Newtonian², with uniform viscosity and locally negligible body forces, i.e. gravity. Under the aforementioned assumptions, the simplified expression of the Navier-Stokes equation is reported in Eq. A.2.

$$\rho \frac{\partial \mathbf{u}}{\partial t} + \rho \mathbf{u} \cdot \nabla \mathbf{u} = -\nabla p + \mu \nabla^2 \mathbf{u} \quad (\text{A.2})$$

In Eq. A.2 p is the local pressure, \mathbf{u} is the local velocity, μ is the fluid viscosity, ρ is the fluid density. The equation can be non-dimensionalized as in Eq. A.3 for generalization (derivation in [38]).

$$\left\{ \begin{array}{l} \frac{1}{St} \frac{\partial \mathbf{u}^*}{\partial t^*} + \rho \mathbf{u}^* \cdot \nabla^* \mathbf{u}^* = -\nabla^* p^* + \mu \nabla^{*2} \mathbf{u}^* \\ \mathbf{u}^* = \mathbf{u}/U \quad \nabla^* \cdot = \frac{1}{l} \nabla \cdot \quad p^* = p/\rho U^2 \\ t^* = t/t_c \quad t_c = \min(l/U, t_{BC})^3 \end{array} \right. \quad (\text{A.3})$$

In Eq. A.3 \mathbf{u}^* is the normalized velocity, p^* is the normalized pressure and t^* is the normalized time. Two nondimensional parameters come from non-dimensionalization: the Strouhal number and the Reynolds number. The first is expressed as $St = t_c U/l$, thus tends to 1 whenever the boundary conditions change more slowly than the characteristic flow time (l/U), and is way lower than 1 in the opposite case. The

²Linear correlation between flow-related viscous stresses and local strain rate for an infinitesimal volume of fluid.

³Minimum between the characteristic time of the flow (l/U) and t_{BC} , i.e. the time over which the boundary conditions change.

Reynolds number express the ratio between the unsteady and convection-related terms and the viscous ones. Actually, $Re < 2000$ is commonly an indicator of laminar flow, controlled by viscous forces, and $Re > 4000$ implies turbulent flow, featuring chaotic changes in pressure and velocity of the fluid.

The gravity force is neglected in Eq. A.2 for analytical derivations involving a small volume of fluid. For a fluid with steady pressure distribution and negligible viscosity, the effect of gravity can be included, leading to Bernoulli’s equation [39]. Bernoulli’s equation, shown in Eq. A.4, describes energy conservation for a fluid element moving across a streamline and includes energy contributions related to pressure, elevation and kinetic energy.

$$\frac{\partial}{\partial s} \left(z + \frac{p}{\rho g} + \frac{u'^2}{2g} \right) = 0 \quad (\text{A.4})$$

In Eq. A.4 s is the curvilinear coordinate of the streamline, z is the elevation, in the context of Earth’s gravity field, g is the gravity constant, p is the pressure, u' is the velocity magnitude. Bernoulli’s equation cannot be applied to micro-channels, where the impact of viscous stress at the boundaries dominates the flow profile and causes a pressure drop between inlet and outlet. For a fluid material in a quasi-static condition, since the impact of the kinetic term is negligible, Bernoulli’s equation can be simplified and thus the pressure can be derived as a function of the elevation.

In practical applications, together with local relations, global relations are convenient to characterize the flow. Among the commonly used global parameters, the volumetric flow rate describes the amount of fluid passing through a reference surface Σ and is defined in Eq. A.5.

$$Q = \iint_{\Sigma} \mathbf{u} \cdot \hat{\mathbf{n}} \, d\Sigma \quad (\text{A.5})$$

In Eq. A.5 \mathbf{u} is the speed of a infinitesimal element of the surface Σ and $\hat{\mathbf{n}}$ is the versor normal to the surface.

The design of this work features a micro-channel, a standard passive component of microfluidic devices, and two reservoirs. The pressure driving the liquid flow between the two reservoirs, having different liquid levels, is extracted by employing Bernoulli’s equation in each reservoir. Focusing on the microchannel, under the hypothesis of laminar flow, the flow profile inside a tube with circular cross-section is described by the Poiseuille equation (Eq. A.6), derived through geometrical approximations from Eq. A.2.

$$u_{axial} = -\frac{1}{4\mu} \frac{\partial p}{\partial z} (R^2 - r^2) \quad (\text{A.6})$$

Since viscous effect are dominant, the pivotal boundary condition for deriving Eq. A.6 is the no-slip one. Being real surfaces rough, fluid molecules colliding on

them are randomly scattered, on average resulting in a null component of the velocity normal to the walls. The resulting flux profile is parabolical, having zero total velocity at the walls and a maximum at the center of the tube (see Fig. A.1). By spatially integrating the flow profile at first across the section, then across the channel length (for a long channel, i.e. $R \ll L$ and $R/L \ll Re^{-1}$), the Hagen-Poiseuille law, a relation between flow rate and pressure, can be extracted (Eq. A.7).

$$\Delta p = R_{hyd}Q = \frac{8\mu L}{\pi R^4}Q \quad (\text{circular cross-section}) \quad (\text{A.7})$$

Although being derived for a cylindrical channel, the Hagen-Poiseuille law can be extended. The proportionality constant R_{hyd} between pressure drop and flow rate is named hydraulic resistance, depends on the shape of the micro-channel sections and may be analytically derived for constant cross-sections and regular shapes. For a channel with a rectangular section, an analytical approximation is provided in Eq. A.8

$$R_{hyd} \approx \frac{12\mu L}{wh^3(1 - 0.630h/w)} \quad (\text{A.8})$$

In Eq. A.8 μ is the dynamic viscosity, w , h and L are respectively channel width, height and length.

A.2 Materials

The materials used for microfluidic devices underwent a large transition over the years. Early microfluidic devices were fabricated from silicon (use of well-known clean-room techniques) and glass (early interest on electrophoretic phenomena). However, the related fabrication methods were expensive, both are brittle materials, silicon

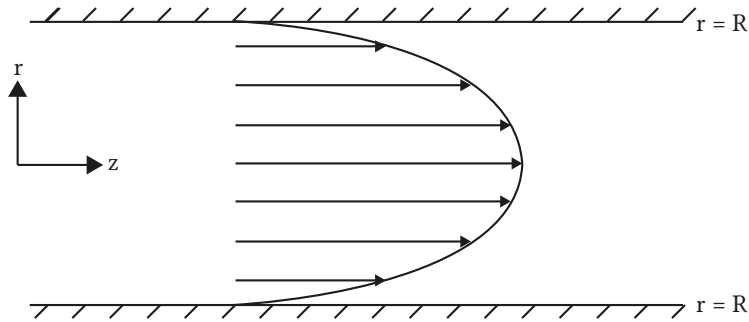


Figure A.1. Poiseuille flow in a circular tube (inspired from [38]).

is opaque. Therefore, soon after being developed, PDMS⁴ rapidly overcame them, becoming a pivotal material and enabling the growth of the field due to:

- The relatively easy and cheap set-up for fabricating a limited amount of devices
- The ability to tune PDMS hydrophobic surface properties
- The simple bonding to glass, PDMS and other materials
- The elasticity, favouring demolding.

However, PDMS still presents several limitations, such as leaching of uncrosslinked oligomers from the curing process into solution, small molecules absorption and vapour permeability. Moreover, PDMS is not easily scalable and is not biocompatible for some applications, despite being generally referred to as a biocompatible material. Therefore, other thermoplastic materials, which can be fabricated through high-throughput methods, are being considered. Materials such as polystyrene, polymethyl methacrylate (PMMA) and polycarbonate, which more suitably meet the requirements of some biological assays are now considered by researchers, even if the material change often implies to re-think design of components. [20]

A.3 Common issues

During fabrication and usage of a microfluidic chip, depending on the material of choice, multiple issues need to be addressed. Bonding is a fundamental issue. Despite bonding is straightforward for PDMS, early microfluidic devices had non-trivial bonding protocols for closing micro-channels [20] and stacked topologies with new thermoplastic materials may share similar bonding problems, since a standard solution for bonding is not always available.

Due to the small dimensions of the components, bubble trapping is a significant problem in many designs, especially for biological assays, and should be limited to ensure correct functioning. Bubbles may be injected during the loading or generated due to variations in temperature and pressure, affecting gas solubility. In this work, pre-heating of the medium and usage of an incubator limited the amount of bubbles in the system, however bubble formation during the loading could not be reliably avoided for the unpunched feature in the last version of the chip, a dead area (see comment in [Sec. 3.3](#)).

Finally, surface properties need to be considered for proper filling of microchannels. To ensure filling of the microchannels on a time-scale compatible with the required loading time (see [Sec. B.4](#)), either modification of surface properties or coating are

⁴Polydimethylsiloxane, an optically transparent, gas- and vapour-permeable elastomer, patterned through soft lithography.

viable solutions. Being biocompatibility a pivotal requirement in biological assays, surface coating may be also needed to render the chip material biocompatible (e.g. to prevent sticking cells or evaporation from micro- and nanolitre fluid volumes, detrimental for cell microenvironment). [20] In this work, an adequate hydrophilicity of the channel was ensured through a plasma treatment of the FlexdymTM component prior-to-assembly.

Appendix B

Capillary effects

As described in [Annex A](#), the physics in microfluidics is to a large extent the same as in the macro-world. However, due to scaling of dimensions, new effects are dominating. Capillary forces (surface forces) stand out among the effects that become more relevant at the micro-scale and may be flow-driving forces or adverse effects. To understand the effects of concern, the fluid need to be analyzed from a thermodynamic point of view. Considering a system in thermodynamic equilibrium formed by two phases, one gaseous, the other liquid, the internal energy of the system for may be described by a thermodynamic potential, the Gibbs free energy G , for the following derivations. The thermodynamic parameters of concern are then temperature T , pressure p and number of particles, also expressible in terms of surface area A in the followings. [40]

B.1 Surface Tension

Surface tension (γ) is the central concept for the capillary effects. Surface tension is defined at the interface between two phases, since the binding energy of a molecule at the interface is different with respect to a particle in the bulk. Actually, as depicted in [Fig. B.1](#), a molecule in the bulk forms chemical bonds with all the molecules in

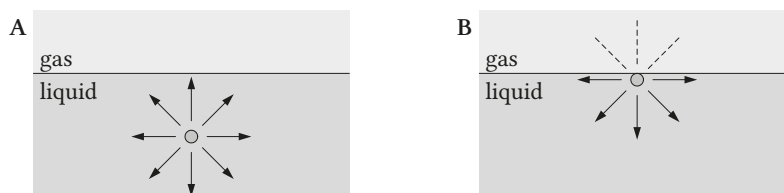


Figure B.1. Cause for surface tension in a liquid-gas interface A) Molecule in the bulk: all bonds saturated B) Molecule close to the interface: lacking chemical bonds (dotted lines), increased chemical potential. [40]

the surroundings, whereas some bonds are precluded for a molecule belonging to the surface. Ultimately, the presence of a surface increases the energy the system due to the unsaturated bonds, therefore the surface area is minimized at the thermodynamic equilibrium. By definition, γ is given by [Eq. B.1](#).

$$\gamma \doteq \left(\frac{\partial G}{\partial A} \right)_{p,T} \quad (\text{B.1})$$

The surface tension value depends on the material at both parts of the interface and for most liquids is in the 20 mJ/m² to 70 mJ/m² range at room temperature (72.9 mJ/m² for water/air interface). The concept holds true for two-phase systems including a gas and solid phase, although the expression "surface free energy" is used in these cases.

B.2 Capillary Pressure

Due to surface tension, the presence of a surface pressure may be demonstrated for a curved interface. Assuming the interface as a surface dividing two continuous media and considering a small volume including including this surface, let the surface move by an infinitesimal amount. The variation in surface area due to the displacement δz can be expressed as in [Eq. B.2](#).

$$\delta A = \left(\frac{\delta z}{R_1} + \frac{\delta z}{R_2} \right) A \quad (\text{B.2})$$

where R_1 and R_2 are the radii of curvature of the surface, considered positive if drawn into the air phase. Under the assumption of quasi-static thermodynamic process, the variation of Gibbs potential in response to an infinitesimal change of the thermodynamic parameters must be equal to zero (demonstration in [\[40\]](#)). If neglecting the gravity force, the Gibbs potential variation due to area and volume variations can be also expressed as in [Eq. B.3](#).

$$\begin{aligned} \delta G &= \delta G_{liquid\,expansion} + G_{gas\,compression} + \delta G_{surface} = \\ &= p_{liquid} A \delta z - p_{gas} A \delta z + \gamma \delta A = \\ &= A \delta z \cdot \left[\gamma \left(\frac{1}{R_1} + \frac{1}{R_2} \right) + p_{liquid} - p_{gas} \right] = 0 \end{aligned} \quad (\text{B.3})$$

By imposing the potential variation equal to zero in [Eq. B.3](#), the Young-Laplace equation ([Eq. B.4](#)) is derived.

$$\Delta p_{capillary} = p_{gas} - p_{liquid} = \gamma_{LG} \left(\frac{1}{R_1} + \frac{1}{R_2} \right) \quad (\text{B.4})$$

The Young-Laplace equation recognizes and quantifies the presence of a pressure drop across the interface, which can be eventually used as driving force. This law was derived with the approximation of negligible impact of gravity and under this assumption the surface tends to have a spherical shape (minimum surface at parity of volume). At the macro-scale, the liquid-gas interface is notably flat due to the gravity contribution, a volume force, so as to minimize the gravitational potential energy for the liquid.

For the example problem of the interface shape in a cylindrical capillary, surface effects dominate if the radius of the capillary is well below a characteristic length l_{cap} , 2.7 mm for a air-water interface. In this work, capillary pressure was not required as a driving force and furthermore a non-zero difference between capillary pressures was detrimental for the correct functioning of the chip (see Sec. 2.4.6). A non-negligible capillary pressure was observable in the reservoirs since the reservoir radius was around 2.25 mm, hence below the capillary length l_{cap} ¹.

B.3 Contact angle

A final notion is needed to explain the impact of capillary effects in microfluidics, the contact angle, an useful parameter to describe the static or quasi-static equilibrium of a three-phase system composed by a gaseous, a liquid and a solid phase. Considering an ideal atomically flat solid surface, as in Fig. B.2, the contact angle in the 2D

¹The ratio between reservoir radius and capillary length is still close to unitary, therefore both volume and surface effects play a role in determining the surface shape. However, for explanatory purposes, in Sec. 2.4.6 capillary pressures are expressed for dominant contribution of surface effects.

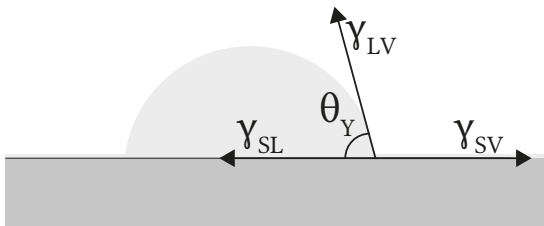


Figure B.2. Scheme for Young contact angle of a three-phase system: gas phase, flat solid surface, liquid droplet.

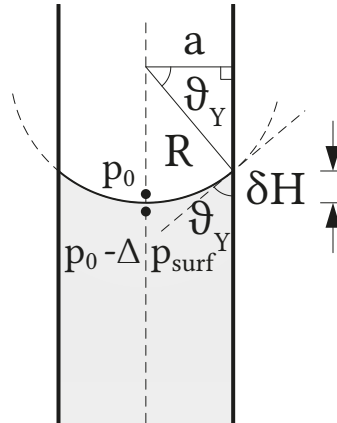


Figure B.3. Outline diagram of cylindrical capillary: relation between capillary pressure and contact angle (edited from [40]).

projection can be seen as the angle between the liquid-solid contact line and the vapour-liquid one and is the result of a balance among the surface tensions. For a system of this kind, through a similar procedure with respect to Eq. B.3, the Young’s equation (Eq. B.5) can be derived.

$$\cos(\theta_Y) = \frac{\gamma_{SV} - \gamma_{SL}}{\gamma_{LV}} \quad (\text{B.5})$$

In Eq. B.5 θ_Y is the contact angle, γ_{SV}, γ_{SL} and γ_{LV} are respectively the solid-vapour, solid-liquid and liquid-vapour surface tensions. The solid-vapour tension is not equal to the surface-vacuum one since the first is influenced by the presence of a wetting or adsorption film. Systems of this kind can then be classified with respect to the contact angle into hydrophilic ($\theta < 90^\circ$) and hydrophobic ($\theta > 90^\circ$). The contact angle notion has numerous applications, one of them is micro-channels filling. Under dominance of surface effects, the curvature radius of the liquid-gas interface can be derived from the contact angle, as shown in Fig B.3. The capillary pressure can be shown to be higher at low contact angles and to decrease down to zero as the contact angle approaches 90° , as expressed in Eq. B.6 for a cylindrical capillary.

$$\Delta p_{capillary} = \gamma \left(\frac{1}{R_1} + \frac{1}{R_2} \right) = \frac{2\gamma_{LG}\cos(\theta_Y)}{a} \quad (\text{B.6})$$

In Eq. B.6 a is the radius of the capillary, θ_Y is the Young contact angle, γ_{LG} is the gas-liquid surface tension, R_1 and R_2 are the radii of curvature of the surface. The water contact angle for a solid phase is commonly considered and consists in the contact angle for a system including the solid phase of concern, a gaseous and a liquid water phase. The filling speed of a micro-channel is driven by capillary forces and is hence dependent on the contact angle. Therefore, in practical applications, a sufficient hydrophilicity of the channel material is required to fill channels without external pumping systems. Some common contact angles are reported in Tab. B.1.

Table B.1. Common liquid-solid contact angles at 20°C . [40] [41]

Liquid	Solid	Water Contact angle
water	SiO ₂	52.3°
water	glass	25.0°
water	Au	0.0°
water	Pt	40.0°
water	PMMA	73.7°
water	PDMS	113.5°

B.4 Impact on this work

For the fabrication of the microfluidic chip of this work, factors affecting the contact angle and surface modification strategies for the solid phase were considered. By looking at the Young equation, an initial consideration about the water contact angle can be made beforehand. Since the contact angle depends on the surface tension between solid and vapour, the thickness of the wetting film may play a role as a source of variability. The wetting film thickness may vary depending on the saturation of the gas with the liquid molecules and on the history of formation of the contact lines of the three-phase system [26]. Differences in water contact angle due to the dependence on film thickness may be the source of the asymptotic capillary stop reported in [Sec. 2.4.6](#).

The contact angle obtained through the Young equation refers to an atomically flat surface. Roughness can change the effective water contact angle and the roughness impact, for protrusions lower than the capillary constant and curvature radius², is described by the Wenzel relation.

$$\cos(\theta_W) = r_W \cos(\theta_Y) \quad (\text{B.7})$$

In the latter θ_W is the Wenzel contact angle, θ_Y is the contact angle from the Young formula, r_W is the ratio between the actual surface area and the surface area for a flat solid phase. The impact of roughness could not be assessed in this work due to the absence of reliable measures of the roughness for the laser-cut PMMA surface.

Hydrophilicity may be tuned through surface treatment of the solid phase to fit the needs of the application. Coating is a common method to affect the water contact angle, e.g. Biolipidure®-206 in this work, as the coating material dominates the surface properties of the solid phase. Chemical vapour deposition processes and strategies involving physisorption of the coating material (e.g. Biolipidure®-206) are widely used to perform the coating process.

Plasma treatment is the standard way of tuning PDMS hydrophilicity and can be used for other thermoplastic polymers, materials of interest in microfluidic devices (see [Annex A.2](#)). For thermoplastic polymers, new functional groups are created on the surface upon plasma treatment, namely hydroxyl (-OH) and carboxyl (-COOH) groups, varying the surface tension at the interface with other phases. Nevertheless, most polymers partially or fully lose the acquired hydrophilicity as time progresses, resulting in hydrophobic recovery. Various phenomena induce hydrophobic recovery, e.g. reorientation of polar groups at the surface into the bulk, diffusion of modified species from the surface to the bulk and diffusion of non-modified species from the bulk

²This condition is verified in the cylindrical reservoirs of this work, since the curvature radius for pristine PMMA and 4.5 mm reservoir diameter is higher than 1 m.

to the surface. [42] Moreover the time-scale of hydrophobic recovery not only changes depending on the dominant phenomenon, but also whether the material is kept in dry or wet conditions after treatment (e.g. from tens of minutes in dry conditions to days in wet conditions for PDMS [27]).

In this work, during chip development, a significant difference in capillary pressures of the two reservoirs was an undesired effect. Different water adsorption between the two reservoirs and different hydrophobic recovery for wet and dry conditions could cause a discrepancy in the liquid levels of the two reservoirs. Coating was found to be the most effective strategy to tune the surface properties so as to guarantee a negligible capillary stop.

Appendix C

Demodulation

Accurate measuring of slight variations in physical quantities are often challenging, since the signal can be dominated by external interference in the form of noise. A common strategy to recover the signal of concern is the modulation of the excitation signal at a frequency sufficiently higher than the bandwidth, followed by demodulation at the same frequency.

From the analytical point of view, both amplitude modulation and amplitude demodulation consist in multiplying the input signal for a reference signal, commonly a sinusoidal wave. Taking as example the sinusoidal input:

$$v_{IN}(t) = A \sin(2\pi f_M t + \phi) \quad (\text{C.1})$$

the output signal after demodulation at f_M is:

$$\begin{aligned} v_{OUT}(t) &= (+A \sin(2\pi f_M t + \phi)) \cdot \sin(2\pi f_M t) \\ &= \frac{A}{2} \cos(\phi) - \frac{A \cos(2 \cdot 2\pi f_M t)}{2} \cos(\phi) + \\ &\quad + \frac{A \sin(2 \cdot 2\pi f_M t)}{2} \sin(\phi) \end{aligned} \quad (\text{C.2})$$

The output signal v_{OUT} can be then low-pass filtered to keep the DC component, allowing to investigate the properties of the input signal v_{IN} at f_M . Phase and amplitude of the input signal can be recovered by simultaneously multiplying the input signal for a second reference signal, in phase-quadrature with the first reference signal. Amplitude and phase detection in a lock-in amplifier are performed as shown in [Fig. C.1](#).

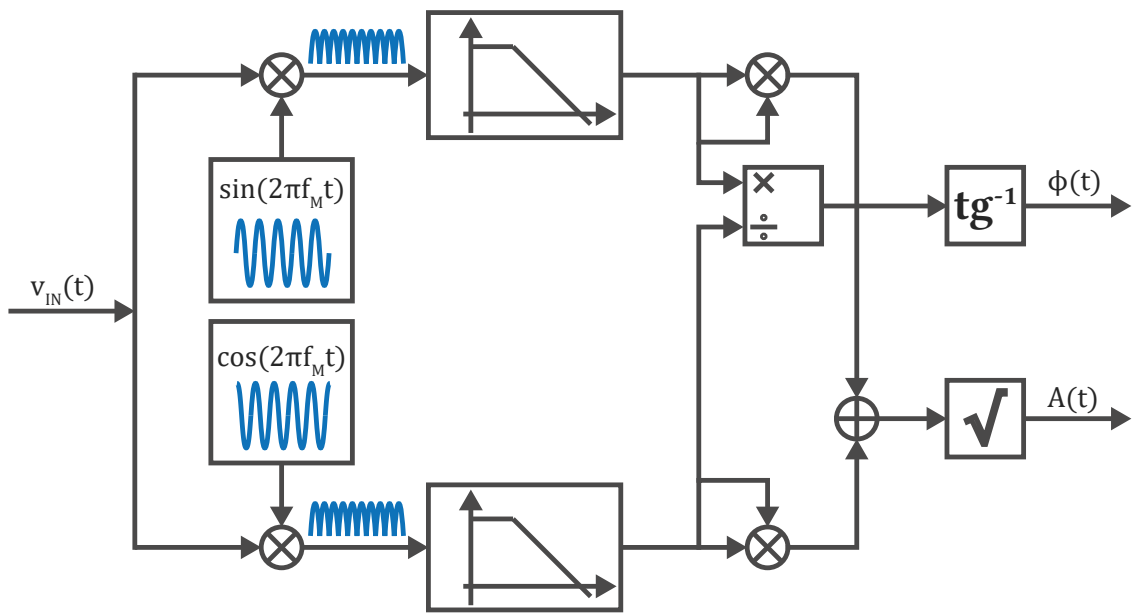


Figure C.1. Demodulation in a lock-in amplifier.

Appendix D

Simulink models insights

As asserted in [Sec. 2.9](#), the measurement system was modeled to select suitable electronic components to use in the new platform for NTS viability readout. The system was replicated as a Simulink[®] model, shown in [Fig. D.1](#) and including the main sources of noise, and was operated through a Matlab[®] script.

The uniform quantization model was used to describe ADC and DAC noise. In the uniform quantization model the step size between two encoded values, Δ , is the full-scale voltage divided by the number of levels. Subsequently, the quantization error is an uniformly distributed random value in a symmetric interval of half a step size

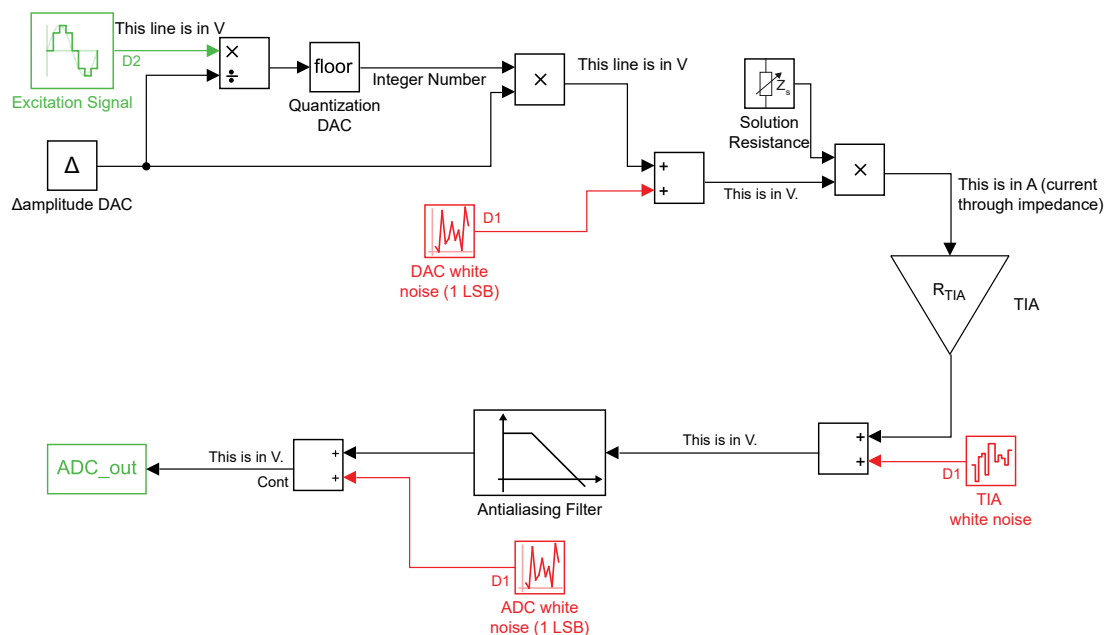


Figure D.1. Simulink model: block diagram.

around the discrete level. For an N-bit quantizer, Eq. D.1 can be derived [43].

$$\left\{ \begin{array}{l} \Delta = \frac{V_{Fs}}{2^N} \\ e_k(nT_s) \in \left[-\frac{\Delta}{2}; \frac{\Delta}{2} \right] \\ P_e = \frac{\Delta^2}{12} \\ S_e(f) = \frac{2P_e}{f_s} \mathbb{1} \{0 \leq f \leq f_s/2\} \end{array} \right. \quad (\text{D.1})$$

In Eq. D.1 V_{Fs} is the ADC-DAC full scale voltage range, $e_k(nT_s)$ is the quantization error for the k_{th} level, P_e is the noise variance and S_e is the noise power spectral density, $\mathbb{1} \{0 \leq f \leq f_s/2\}$ is the rectangular window function for the $[0; f_s/2]$ frequency interval, f_s is the sampling frequency.

The Simulink[®] model features a signal generator, producing a 500 kHz sinusoid of 200 mV_{pp}, a DAC, a lumped resistor, representing the electrolyte resistance, a transimpedance amplifier, a low pass filter and an ADC. An ADC range of 2 V_{pp}, representing a large number of components on the market, was chosen. The excitation signal amplitude was a design requirement, therefore the DAC range was selected accordingly as the peak-to-peak excitation voltage. A solution resistance of 3.3 kΩ was selected, compatibly with Sec. 2.8, and a TIA current amplification of 33 kΩ was chosen to fully occupy the ADC range. The parameters used in each block of Fig. D.1 are shown in Tab. D.1.

The control Matlab[®] script was written to implement down-sampling, required in practical applications to lower the rate of data transfer to the control PC. The overall simulation time was divided into time intervals, equal to the down-sampling period, in which to run the Simulink[®] model. For each time interval, the signal from the ADC was demodulated at 500 kHz, to obtain the amplitude at the demodulation frequency, and the average value, the DC component, was extracted. The down-sampled signal was taken as the collection of the values extracted for each time interval.

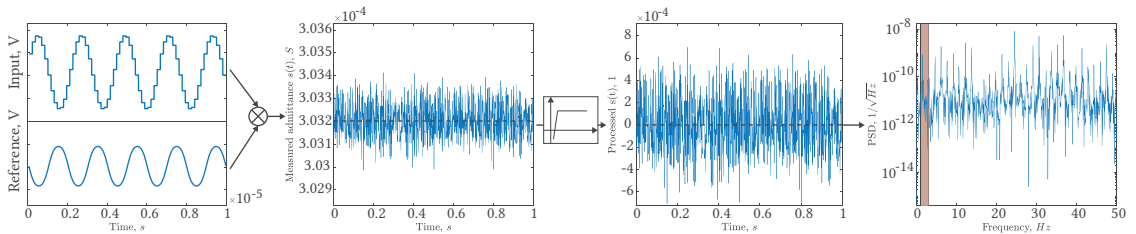


Figure D.2. Outline of data processing: from ADC sampling to noise level.

The baseline of the signal was computed by averaging the down-sampled signal. Finally, the signal related to NTS viability was obtained by dividing and subtracting the baseline to the down-sampled signal. The power spectral density of signal related to NTS viability was computed and the noise level was evaluated by integrating the power spectral density in the 1 – 3 Hz range. The obtained noise level was then considered for component selection. The outline of signal processing is shown in Fig. D.2.

From an analytical point of view the overall noise of the signal related to NTS viability, including the quantization noise but excluding sample quantization and down-sampling, may be expressed as the sum of white noise contributions in Eq. D.2.

$$\left\{ \begin{array}{l} P_n = \frac{1}{v_{\text{baseline}}^2} \left(\frac{\Delta_{ADC}^2}{12} + \frac{\Delta_{DAC}^2}{12} \cdot \frac{R_{TIA}^2}{R_{sol}^2} + \frac{f_s}{2} \left(e_{out,V}^{TIA} \right)^2 \right) \\ S_{n,baseband} = \frac{1}{v_{\text{baseline}}^2} \left(\frac{\Delta_{ADC}^2 \cdot 2}{12 \cdot f_s} + \frac{\Delta_{DAC}^2 \cdot 2}{12 \cdot f_s} \cdot \frac{R_{TIA}^2}{R_{sol}^2} + \left(e_{out,V}^{TIA} \right)^2 \right) \end{array} \right. \quad (\text{D.2})$$

In Eq. D.2 P_{noise} is the overall power of noise, $S_{n,baseband}$ is the relative PSD height, R_{TIA} is the transimpedance gain, R_{sol} is the solution resistance, f_s is the sampling frequency, $e_{out,V}^{TIA}$ is the output voltage noise of the transimpedance amplifier, v_{baseline} is the voltage baseline, taken as the average demodulated amplitude over the whole measurement time, referable to the average solution impedance.

In the Simulink[®] model the effects of down-sampling and quantization increase the measured noise, narrowing down the feasible combinations of sampling frequency and number of bits for ADC/DAC. The trade-off points for down-sampling at 1 kHz are outlined in Fig. 2.10. The complete set of noise levels is reported in Fig. D.3. Re-sampling by discarding 31 out of 32 data points lead to more strict requirements as the noise levels, shown in Fig. D.4, increase. The latter condition requires limited data exchange with the control PC and corresponds to an effective sampling rate for chamber of 31.25 Hz, sufficient for capturing the NTS movements (10 Hz is selected as the hard limit to safely capture parasite movements up to 4 Hz).

The impact of down-sampling frequency was considered separately. For a single combination of ADC/DAC number of bits and sampling frequency, i.e. 14 bits and 4 MHz, the noise level was computed at increasing down-sampling frequency in the 32 Hz to 20 000 Hz frequency range. The results are shown in Fig. D.5. An higher down-sampling frequency in the range of concern lead to a lower noise level. Nonetheless, the down-sampling frequency needs to be significantly smaller than the excitation frequency, so as to include a sufficient number of periods of the input signal for amplitude extraction (20 kHz is acceptable as coincides with 25 periods).

In Sec. 2.10 components were chosen according to the aforementioned results. Nevertheless comparison with simulation data was not possible due to nonidealities in the generation of the excitation signal, leading to low frequency components in the PSD of the demodulated signal above the white-noise baseband.

Table D.1. Simulink® model parameters.

Parameter	Value
Number of bits ($NBIT$)	6, 8, 10, 12, 14
Sampling frequency (f_s)	4, 10, 20, 30, 50, 125 MHz
Down-sampling frequency (f_s)	1 kHz
Excitation Signal: Amplitude	200 mV _{pp}
Excitation Signal: Frequency	500 kHz
Excitation Signal: Sample Time	$1/f_s$
DAC White Noise: Maximum/Minimum	$\pm \frac{200 \text{ mV}_{pp}}{2^{NBIT}}$
DAC White Noise: Sample Time	$\frac{2\pi}{100f_s}$
Solution Resistance	3.3 k Ω
Δ amplitude DAC	$\frac{200 \text{ mV}_{pp}}{2^{NBIT}}$
ADC White Noise: Maximum/Minimum	$\pm \frac{2 \text{ V}_{pp}}{2^{NBIT}}$
ADC White Noise: Sample Time	$\frac{2\pi}{100f_s}$
TIA White Noise: PSD Baseband	0.01 $\mu\text{V}_{rms}^2/\text{Hz}$
TIA White Noise: Sample Time	$\frac{2\pi}{100f_s}$
Anti-aliasing filter: Cutoff Frequency	$\frac{f_s}{2}$
Anti-aliasing filter: Type	Butterworth
Anti-aliasing filter: Order	2
TIA Gain	33 k Ω

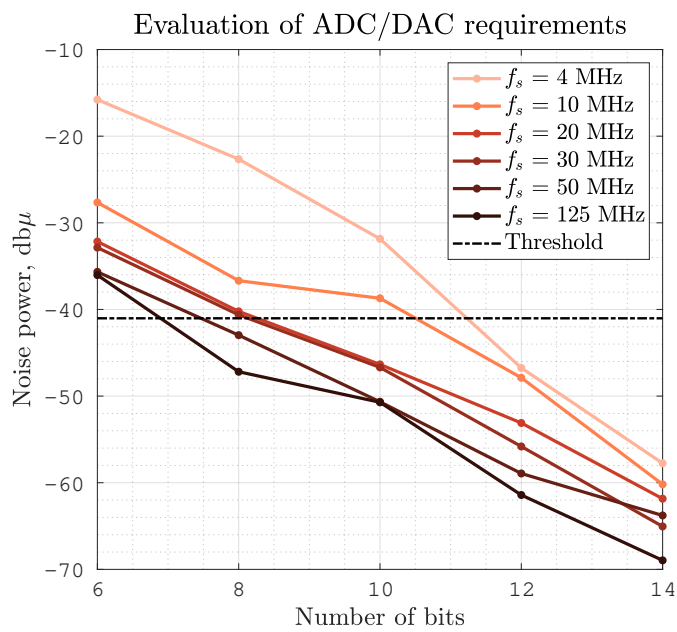


Figure D.3. Noise level as a function of the ADC/DAC number of bit. Down-sampling at 1 kHz.

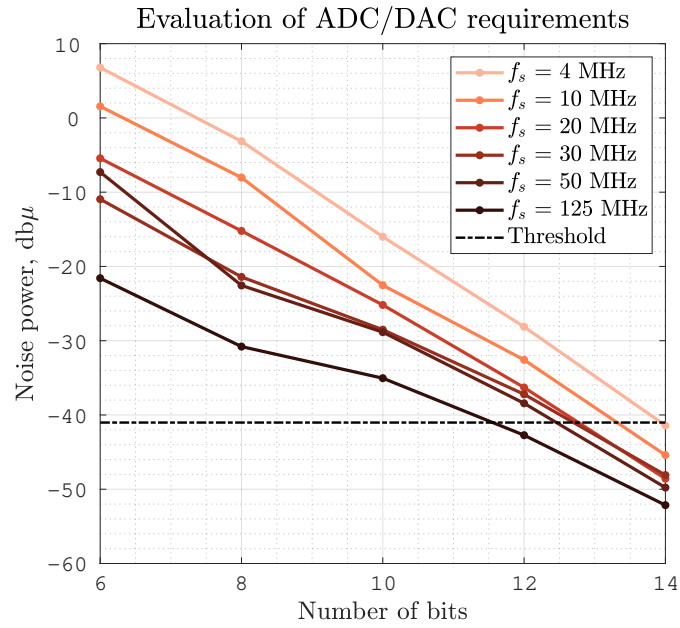


Figure D.4. Noise level as a function of the ADC/DAC number of bit. Down-sampling at 1 kHz and re-sampling at 31.25 Hz by discarding data.

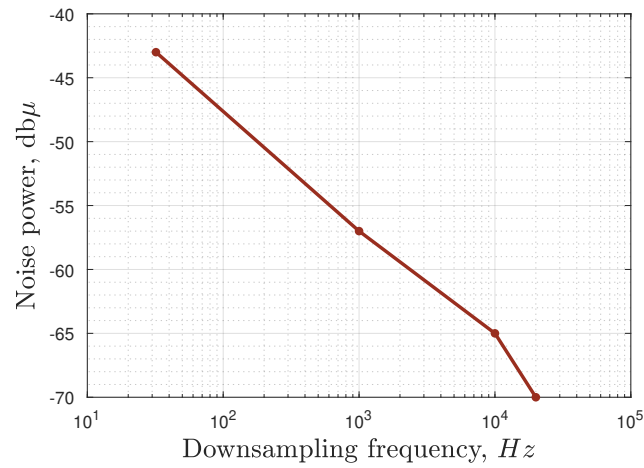


Figure D.5. Noise level as a function of the down-sampling frequency. Sampling frequency and ADC/DAC number of bits respectively 4 MHz and 14 bits.

Appendix E

Comsol models insights

As expressed in [Sec. 2.3](#), Comsol[®] simulations were carried out to find the flow and concentration profile. To simplify the problem, two sub-models were created, addressing different issues. The conceived design features a channel connecting two cylindrical reservoirs. The volumes of liquid in the two reservoirs are uneven at the initial time of the assay, therefore, for simplicity, the more filled one will be addressed as source reservoir, whereas the other will be addressed as sink reservoir. For the sake of this work, 3 Comsol modules were used:

- Laminar flow module: as discussed in [Annex A](#), microfluidic devices work under laminar regime, so appropriate simplifications were made with the same hypothesis as in [Annex A.1](#) for [Eq. A.2](#), but locally including body forces, i.e. the gravity force. This module is used to compute velocity and pressure field for the flow of a single-phase fluid in laminar flow regime. For both sub-models:
 - water density and viscosity at the reference temperature were used in the equations;
 - a no-slip boundary condition was applied on all the walls;
 - an open boundary condition was applied on the free surfaces of the reservoirs (null normal stress);
 - the initial values of the pressure were defined in accordance with the gravitational field and the velocity was initialized to zero within the domains.
- Transport of diluted species module: this module is used to calculate the concentration field of a dilute solute (drug) into a solvent. Fick's diffusion equations were implemented, with the addition of an advective term coming from the coupling with the laminar flow module. For both sub-models:
 - water was chosen as solvent;

- a representative solute having a diffusion coefficient close to the one of penicillin¹ was selected;
 - the sink reservoir water was initialized with the desired concentration of solute, the source reservoir and the channel with no solute at all;
 - all exterior boundaries were initialized with a no-flux boundary condition (no solute mass flux).
- Moving Mesh module: controlling the spatial frame, used in a model where geometry changes due to motion of solid boundaries or deformation of solid domains. Only present in the second sub-model (boundary conditions in the followings).

Finally, specific boundary conditions were present in each module to fully exploit symmetries in the geometry, reducing the computational burden.

E.1 Sub-model I: preliminary information

During the time of the assay the volumes of the reservoirs change over time. To limit the computational burden tied with a varying geometry in Comsol[®], the whole chip at the initial time of the assay was considered to extract some of the information.

¹Most drugs of interest share similar molar mass and dimensions, therefore, as a first approximation, similar diffusion coefficients.

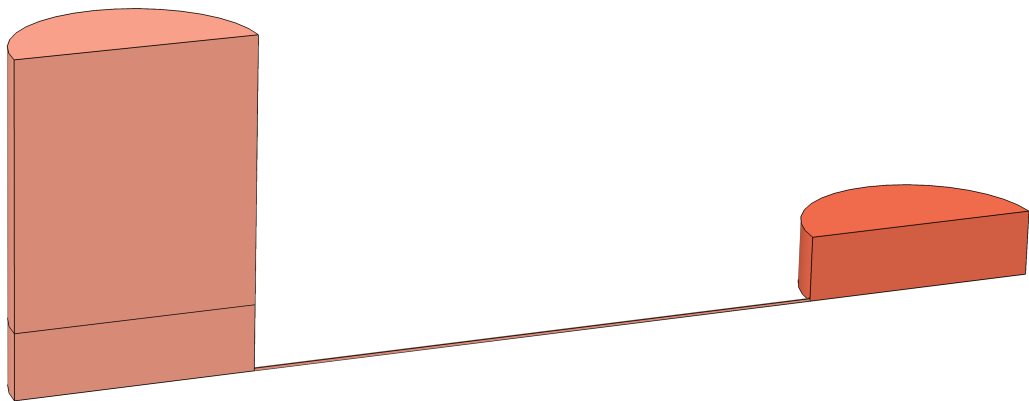


Figure E.1. Comsol[®] sub-model I: geometry.

A sub-model representing the chip at the start of the assay, whose geometry is shown in Fig. E.1, was created. At first, a stationary analysis, only featuring the laminar flow model, was performed. A stationary analysis of the flow lead to a more accurate estimation of the hydraulic resistance to use in the Hagen-Poiseuille equation and to the precise evaluation of the pressure gradient between the inlet and the outlet of the channel. Depending on the conditions of the fluid, the pressure could be different within the inlet or the outlet, but a nearly constant pressure was observed over each one of the two surfaces. The computation of the hydraulic resistance was performed by computing the difference between the average pressure at the inlet and at the outlet, then dividing it by the flow rate (applying Eq. A.5 at the inlet). The hydraulic resistance values obtained through the simulation and the analytical estimations, computed through the expression in Annex A.1, are available in Tab. E.1.

Subsequently, a preliminary analysis was performed to introduce an initial simplification. A priori, both advection and diffusion should be considered across the channel. However, whenever one of the two contributes is dominating, ruling out the negligible phenomenon for reasonably small simulation times leads to less computational burden and equally valid results. The Péclet number (Pe), i.e. the ratio between the advection velocity and the diffusive one (see Eq. E.1) is an handy parameter to identify the dominant phenomenon.

Table E.1. Geometrical parameters for Comsol® simulations

Channel section, μm	Channel length, mm	Reservoir radius, mm	Analytical estimation R_{hyd} , $\text{kg}/\text{mm}^4\text{s}$	R_{hyd} extracted from Comsol® simulation, $\text{kg}/\text{mm}^4\text{s}$
50x75	7	2.25	10.7	15.1
	9		13.7	19.2
	11		16.8	23.4
	15		22.9	31.5
	19		29.0	40.4
	23		35.1	49.0
	27		41.2	57.4
	31		47.3	66.2
	35		53.4	73.9

$$\begin{aligned}
 Pe &= \frac{\text{advection velocity}}{\text{diffusion velocity}} = \frac{c|\mathbf{u}|}{D\nabla c} \text{ (local)} \\
 &= \frac{UL}{D} \text{ (global)}
 \end{aligned}
 \tag{E.1}$$

In Eq. E.1 $|\mathbf{u}|$ is the absolute value of the local velocity, D is the diffusion constant of the species of concern, c is the local concentration, L and U are respectively the characteristic length and speed for the system of concern (see Annex A). Many microfluidic species transport systems reside in the limit of laminar flow and high Péclet number, making straightforward to isolate chemical species but slowing down the mixing of species. [38] The same applies for the micro-channel in the system of concern. Considering a channel length of 11 mm, the range of Péclet numbers for the channel alone corresponding to the initial flow rate (having a reservoir diameter of 4.5 mm) and to one hundredth of the initial flow rate was computed.

$$Pe_{channel} = \frac{Q}{w_{channel} \cdot h_{channel}} \cdot \frac{l_{channel}}{D} = \frac{1 - 100 \text{ nL min}^{-1}}{50 \mu\text{m} \cdot 75 \mu\text{m}} \cdot \frac{11 \text{ mm}}{650 \mu\text{m}^2 \text{ s}^{-1}} = 80 - 8000$$

Being the Péclet number for the channel way above the unity for most values of the volumetric flow rate, drug advection is expected to be dominant in the channel. As an additional way to show that diffusion within the channel is negligible, a time-dependant simulation in the worst case scenario was carried out, isolating the contribution of diffusive mixing across the channel to the concentration in the reservoirs and keeping the initial volume mispropotion. Specifically, only the transport of diluted species module was used, therefore no advective flux was imposed across the channel. The average concentration in each of the two reservoirs remained constant within a 48-h time span. Subsequently, advection may be solely considered to evaluate the concentration profile over time in the sink reservoir.

E.2 From Model I to Model II

The first sub-model alone is not sufficient to assess the concentration profile in each point of the sink, specifically at the bottom, where *S. mansoni* larvae should be located. Although the geometry can be varied in Comsol[®], model optimization is needed to successfully couple the 3 required modules. Therefore, the idea behind the second sub-model was to reduce complexity by only including the sink reservoir and the final part of the channel, thus facilitating the optimization process and reducing the computational burden. Naturally, the correct flux profile needs to be imposed at the cut end of the channel. Therefore, the flow rate, as a function of time and initial conditions, was computed separately, then inserted in the form of a fully developed flow boundary condition on the cut end.

The computation of the flow profile was performed as in the followings. As pointed out in [Sec. 2.1](#), having two equal reservoirs, in terms of material and dimension, and atmospheric pressure on the free surfaces of both reservoirs, the asymptotic volumes in the two reservoirs should match. With no apparent reason to assume a mismatch in the capillary pressures at this stage of simulations, only the gravity field is acting. Bernoulli's equation without the kinetic term was considered in each reservoir to extract the time trend of the pressure difference driving the flow. Equations and boundary conditions are shown in [Eq. E.2](#).

$$\left\{ \begin{array}{l} \frac{\partial V_{sink}(h_{sink}(t))}{\partial t} = Q(t) = \frac{\rho_{mdm}g}{R_{hyd}} \Delta h(t) \\ \frac{\partial V_{source}(h_{source}(t))}{\partial t} = -Q(t) = -\frac{\rho g}{R_{hyd}} \Delta h(t) \\ V_{sink}(0) = V_{tot} - V_{drug} \quad V_{source}(0) = V_{drug} \\ h_{sink}(t) = h_{final,sink} - \Delta h_{sink}(t) \\ h_{source}(t) = h_{final,source} + \Delta h_{source}(t) \\ \Delta h(t) = \Delta h_{sink}(t) - \Delta h_{source}(t) = 2\Delta h_{sink}(t) \end{array} \right. \quad (\text{E.2})$$

In [Eq. E.2](#) $Q(t)$ is the flow rate as a function of time, g is the gravity constant, ρ_{mdm} is the density of the medium, R_{hyd} is the hydraulic resistance of the channel, V_{tot} is the overall volume of medium, V_{drug} is the volume of medium with a non-zero uniform initial drug concentration, V_{source} and V_{sink} the volumes of liquid in sink and source over time, $h_{source}(t)$ and $h_{sink}(t)$ are the liquid height profiles in the reservoirs and $\Delta h(t)$ is the difference between the two. By observing that $\Delta h_{sink}(t) = \Delta h_{source}(t)$, the equation may be simplified as in [Eq. E.3](#)

$$\left\{ \begin{array}{l} \frac{\partial \Delta h(t)}{\partial t} \frac{\pi r_{res}^2}{2} = \frac{\rho g}{R_{hyd}} \Delta h(t) \\ h_{sink}(t) = h_{final,sink} - \Delta h_{sink}(t) \\ \Delta h_{sink}(t) = \frac{\Delta h(t)}{2} \\ \Delta h(0) = \frac{V_{tot} - 2V_{drug} - V_{channel}}{\pi r_{res}^2} \simeq \frac{V_{tot} - 2V_{drug}}{\pi r_{res}^2} \end{array} \right. \quad (\text{E.3})$$

In [Eq. E.3](#) r_{res} is the radius of the reservoirs. Finally [Eq. E.4](#) is straightforwardly obtained.

$$\left\{ \begin{array}{l} Q(t) = \frac{g\rho_{mdm}}{R_{hyd}} \cdot \frac{V_{tot} - 2V_{drug}}{\pi r_{res}^2} \cdot \exp\left(-\frac{t}{\tau_{adv}}\right) \\ \Delta h(t) = \frac{V_{tot} - 2V_{drug}}{\pi r_{res}^2} \cdot \exp\left(-\frac{t}{\tau_{adv}}\right) \\ \tau_{adv} = \frac{R_{hyd}}{2g\rho_{mdm}} \cdot \pi r_{res}^2 \end{array} \right. \quad (\text{E.4})$$

In Eq. E.4 τ_{adv} is the time constant of advection decay. By substitution, the liquid level in the sink may be obtained. The normalized flow profile over time, multiplied for the initial flow rate from Sec. E.1 to improve accuracy, may be then inserted in the second sub-model.

E.3 Model II: concentration profile

Including the results of [Sec. E.2](#), the second sub-model was created. A representation of the initial geometry of the sub-model is shown in [Fig. E.2](#). For each value of hydraulic resistance, thus channel length, the relative flow profile was imposed as a fully developed flow at the cut end. The moving mesh module was used, enabling the possibility for mesh elements to deform over time. In this specific model the mesh elements stretch in the vertical direction, as the free boundary raises during the simulation time. Parallelepipedal mesh elements were chosen, due to the simple axial deformation and the accordance with the flow profile. The following boundary conditions were applied:

- upper part of the sink reservoir: deformable domain - mesh smoothing type: Yeoh (stiffening factor: 10);
- bottom surface of the deformable domain: fixed displacement (null);
- walls of the reservoir: mesh slip (zero normal velocity of mesh elements);
- free surface: prescribed mesh velocity (derivative of the sink height over time from [Annex E.2](#)).

To reduce the simulation time and improve convergence:

- parallelepiped were used whenever possible, leaving tetrahedra only in the transition region from channel to reservoir (as shown in [Fig. E.3](#));
- the ending part of the channel was filleted ($30\ \mu\text{m}$ filleting radius);
- the initial conditions for the transport of diluted species module were refined, by removing the discontinuity in the initial conditions between channel and

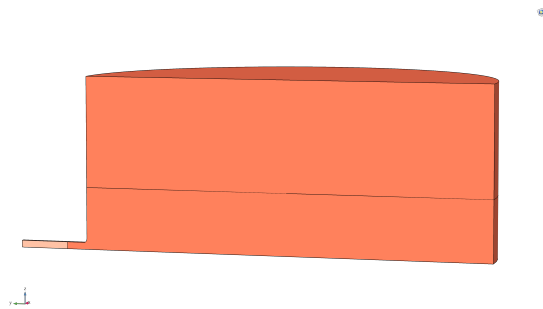


Figure E.2. Comsol[®] sub-model II: geometry.

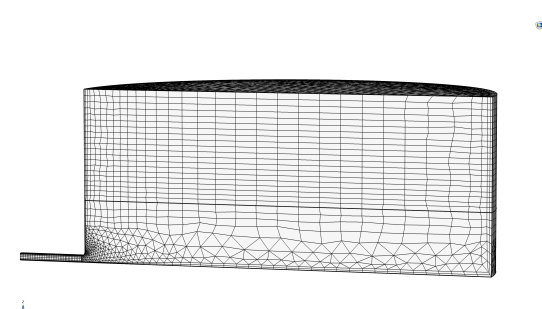


Figure E.3. Comsol[®] sub-model II: mesh.

reservoir. An exponentially decaying profile² from the source concentration of solute to zero was imposed at ending part part of the channel.

The optimized mesh is shown in Fig. E.3. The average concentration profile and the local concentration profiles in three regions of the sink reservoir, labeled in Fig. E.4, were extracted from a 24 h transient simulation. Region *a* and *b* are circular segment, extruded in the vertical direction for 60 μm , capable of hosting 20 NTS (c.a. 100 μm long and 50 μm wide [1]). Region *c* is cylindrical and share the same height and volume as region *a* and *b*.³ For a representative condition, the concentration profiles over time are reported (see Fig. E.5). The half-lives of the four concentration profiles were extracted as functions of the hydraulic resistance of the channel (specifically the channel length was varied, equally valid modifications of height and width may be performed instead). The results are shown in Fig. E.6. A shift for region *a* and *b* with respect to the average concentration profile, independent on the hydraulic resistance, was observed for the considered parameters. Additionally, behaviour of the half-lives was examined while changing the reservoir radius at a fixed hydraulic resistance, keeping identical loading volumes for all conditions (thus a lower radius implies and higher and narrower liquid column). The results of Fig. E.7 highlight a dependency of the half-lives with respect to the reservoir radius and an increasing divergence among region *a*, *b* and *c*. For the lowest reservoir radius, the concentration at the base of the reservoir eventually becomes lower than the average concentration, since the highest part of the reservoir keeps a higher concentration from the start of the assay. Since the *S. mansoni* larvae fall in the lower part of the reservoir, an

²Constant of spatial decay: 25 μm

³ $h_1 = 100 \mu\text{m}$, $h_2 = 1.2 \text{ mm}$, $h_3 = 600 \mu\text{m}$

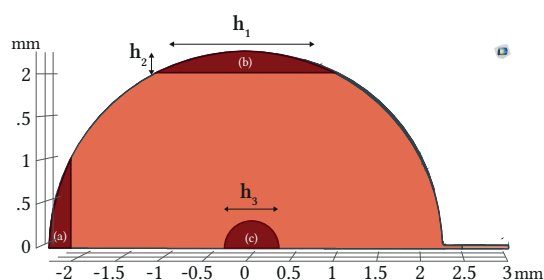


Figure E.4. Reservoir regions for local concentration profile extraction.

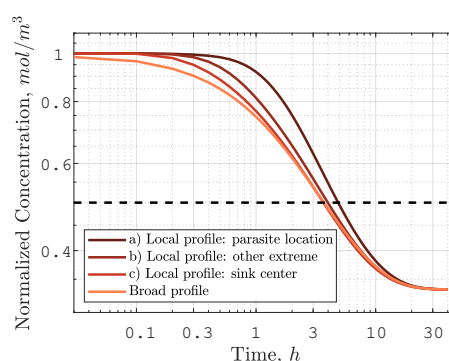


Figure E.5. Exemplar concentration profiles for r_{res} , R_{hyd} and $l_{channel}$ respectively equal to 2.25 mm, 23.4 $\text{kg}/\text{mm}^4\text{s}$ and 11 mm.

higher reservoir radius allows instead to have a slowly-varying concentration profile, dominated by intra-reservoir diffusion, indirectly dependent from the advection of medium and thus less sensitive to potential perturbations of the flux. Specifically, region *a* was selected as the intended location for the parasites.

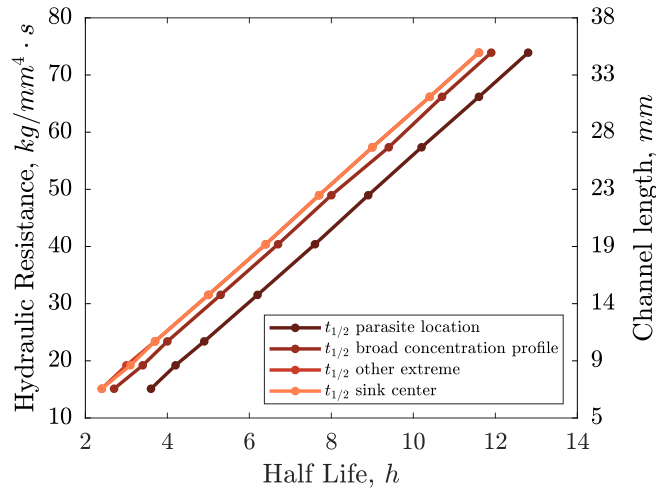


Figure E.6. Half-lives of concentration profiles vs hydraulic resistance at constant reservoir radius.

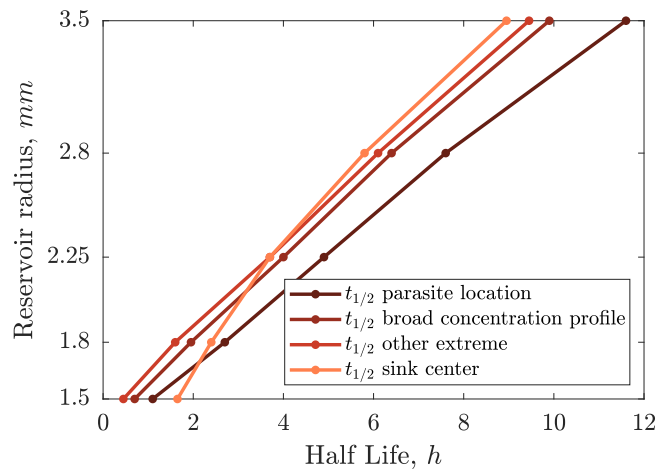


Figure E.7. Half-lives of concentration profiles vs reservoir radius at constant hydraulic resistance.

Appendix F

Protocol for SU8 patterning

An SU-8 mask on a silicon wafer substrate was used for soft-lithography of Flexdym™. A standard UV photolithographic process was used to pattern SU-8. The main steps are the following, also shown in [Fig. F.1](#).

1. Dehydration Bake: 5 min at 200 °C, cleaning with N₂ gun;
2. Spin Coating: deposition of 4 mL of SU8-3050, ramping at 100 rpm/s, spinning for 10 s at 500 rpm, ramping at 500 rpm/s, spinning for 30 s at 3000 rpm;
3. Soft Bake: 20 min at 95 °C, cleaning with N₂ gun;
4. Alignment and Exposure (Süss MicroTec MA/BA8): 2D mask in plastic foil (Micro Lithography Services Ltd) in vacuum contact mode, exposure parameters: I-line, 37% (c'era un valore in watt 970, sarebbe meglio quindi inserire 360 W se ho capito bene) intensity, 9.5 s time-of-exposure, 400 mJ cm⁻² dose;
5. Post-exposure bake 5 min at 95 °C, cleaning with N₂ gun;
6. Development: dipping into mr-dev-600 developer for 10 min, while shaking on a regular basis, cleaning and drying with N₂ gun.

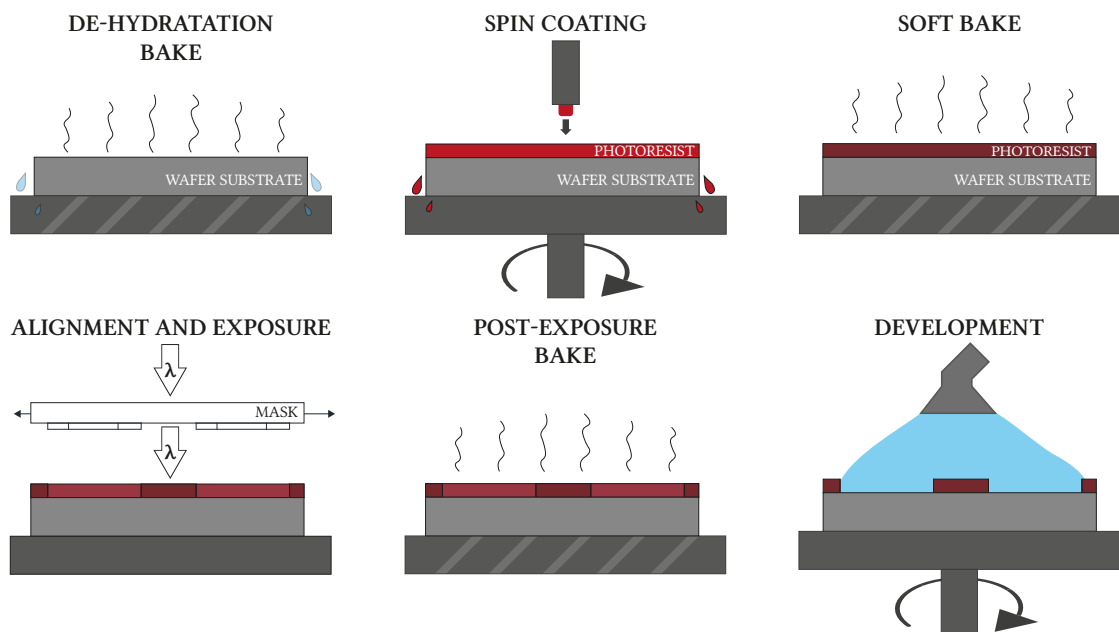


Figure F.1. Steps of SU-8 photolithography.

Appendix G

Half-lives data collection

Pharmacokinetic data were collected for a statistical analysis of compound half-lives in [Sec. 2.2](#). [Table G.1](#) shows, for each compound, the half-life and the relative source. All selected in-vivo studies were performed on humans, with the exception of 7 studies on laboratory animals (marked). Intravenous studies were preferred over studies featuring oral administration, since the extracted half-life may be influenced by prolonged absorption. [[14](#)]

Table G.1: Half life values for MMV compounds

MMV ID	ChEMBL ID	Half life, h	Source
1581035	1170047	0.067	doi: 10.1021/jm100012m
637306	1460	0.5	Drugbank (DB00900)
1580849	59416	0.7	doi: 10.1021/jm00128a043*
2516	1213136	0.76	Drugbank (DB01085)
1578559	996	0.83	Drugbank (DB01331)
2224	1231530	0.9	doi: 10.1016/j.ejmech.2017.03.022
1613559	766	1	Drugbank (DB01597)
637945	403	1	Drugbank (DB09324)
2740	891	1	www.glowm.com/resources/glowm/cd/pages/drugs/c078.html
1582382	339323	1.2	doi: 10.1016/j.ejmech.2017.03.022
1581032	NA	1.35	doi: 10.1093/jac/dkw458
1438	480	1.4	Drugbank (DB00448)
2560	454446	1.4	doi: 10.1128/AAC.01247-07
1782352	196779	1.5	doi: 10.1016/j.bmcl.2006.06.033
2731	1413	1.7	Drugbank (DB01188)
2459	1747	2	Drugbank (DB00684)
637533	295698	2	Drugbank (DB01026)

Table G.1: Half life values for MMV compounds

MMV ID	ChEMBL ID	Half life, h	Source
2780	402487	2.07	doi: 10.1007/s11064-019-02837-x
2169	64	2.25	Drugbank (DB00951)
30787	1618279	2.3	www.mims.com/malaysia/drug/info/revaprazan
1633678	84	2.5	Drugbank (DB01030)
1634556	285833	2.5	doi: 10.1021/jm00008a014*
690467	29609	2.5	doi: 10.1021/acs.jmedchem.6b01834
1961	184	2.75	Drugbank (DB00787)
3137	532	2.75	Drugbank (DB00199)
1613560	1689063	2.85	Drugbank (DB09060)
1761	182	2.9	Drugbank (DB01004)
3738	63	3	doi: 10.1007/BF00314807
51	1753	3	Drugbank (DB01190)
1580497	218394	3.4	Drugbank (DB08873)
687801	44884	3.5	Drugbank (DB00330)
1782355	311300	3.5	doi: 10.1177/00912700022008991
1578884	NA	3.5	doi: 10.1128/AAC.01395-19
4508	1463	3.6	Drugbank (DB01099)
1580495	1464327	4	Drugbank (DB00928)
1580494	231813	4.35	Drugbank (DB05521)
1580502	18442	4.5	Drugbank (DB06809)
1613563	134561	4.61	doi: 10.1093/ofid/ofy003
658803	289228	4.9	doi: 10.1126/science.1160354
690706	440498	5	www.microconstants.com/wp-content/uploads/2020/02/cts-1027-pk-aaps-november2009.pdf
18362	348000	5.25	PubChem (Cinchophen)
1634389	1760434	5.5	doi: 10.1039/C0MD00197J*
1578575	374975	5.5	Drugbank (DB02703)
1782112	141816	5.6	doi: 10.1021/jm030166l
2354	1757	5.7	Drugbank (DB00828)
637659	190561	6	doi: 10.1021/jm050035f
2612	468	6	Drugbank (DB01041)
1581034	3039531	6	doi: 10.1186/s40360-015-0017-x
1782386	1289313	6.2	doi: 10.1021/jm200208d*
1580797	190333	6.4	doi: 10.1177/0091270002250615
1579850	108821	6.6	doi: 10.1124/dmd.108.020479
1578568	3317856	6.6	doi: 10.1093/ofid/ofz360.1344

Table G.1: Half life values for MMV compounds

MMV ID	ChEMBL ID	Half life, h	Source
1593521	515408	6.88	doi: 10.1128/AAC.00951-07
1593517	3545185	7	Drugbank (DB11942)
687798	33	7	Drugbank (DB01137)
1782213	1630216	7.1	doi: 10.1128/AAC.00268-10
688991	1401	7.3	Drugbank (DB00507)
1613562	3884248	7.4	doi: 10.1128/AAC.02414-14
688756	288149	7.5	doi: 10.1016/j.ejps.2020.105421*
2350	561	8	Drugbank (DB00978)
28	22	9	Drugbank (DB00440)
3249	614	9.5	Drugbank (DB00339)
2260	865	9.5	Drugbank (DB00580)
2565	42442	9.75	doi: 10.1128/AAC.02255-18
1578558	1474963	10	doi: 10.1016/B978-0-323-07367-7.00020-0
1782214	93139	10.2	doi: 10.1016/S0960-894X(01)00545-5*
1580483	3960662	10.5	doi: 10.1158/1535-7163.TARG-17-A094
1634071	2062774	11.8	doi: 10.1021/ml2002955
640014	550348	12	Drugbank (DB01609)
690653	1241951	12	Drugbank (DB12070)
1726	24510	12	doi: 10.1002/cpt1973144part1541
1593514	431733	12	ir.stockpr.com/canfite/all-sec-filings/content/0001213900-18-003554/f20f2017_canfitebiopharma.htm
59	319669	14	PubMed Central® (PMC2763313)
1578566	3549142	14.3	doi: 10.1124/dmd.112.050153
1580173	119	15.5	Drugbank (DB01157)
1580796	77305	16.5	Wikipedia (Rubitecan)
2287	498847	17	Drugbank (DB12834)
1581036	90983	17.1	doi: 10.1093/neuonc/nor230
688755	227875	17.2	Drugbank (DB05154)
3297	1276308	18	Drugbank (DB00834)
1580492	3707247	19	Drugbank (DB12612)
637413	1568	20	Drugbank (DB01073)
1578574	1951095	20	Drugbank (DB12329)
637528	22587	21	Drugbank (DB01167)
1581377	1138	22	Drugbank (DB00973)
3143	37161	23	doi: 10.2147/VMRR.S77255*
2722	91	24	Drugbank (DB01110)

Table G.1: Half life values for MMV compounds

MMV ID	ChEMBL ID	Half life, h	Source
1634386	3311228	24	doi: 10.1016/j.bmcl.2014.05.068
637855	959	25.5	Drugbank (DB00478)
9948	941	29	Drugbank (DB00619)
2337	106	30	Drugbank (DB00196)
639951	1908360	30	Drugbank (DB01590)
10036	483254	30	Drugbank (DB06603)
1580478	483	32	Drugbank (DB14126)
637104	990	35	Drugbank (DB01091)
1634359	822	36	doi: 10.1111/j.1365-2133.1992.tb00461.x
687273	561057	61	doi: 10.1016/j.ejmech.2012.02.033
1593515	493982	84	Drugbank (DB09030)
1793	7301	91	doi: 10.1200/JCO.2004.09.096
1634362	294029	96	doi: 10.1128/AAC.01742-09
1634494	1183349	105	Drugbank (DB06636)
1580498	2364624	150	doi: 10.1186/s12944-015-0006-5
3291	960	336	Drugbank (DB01097)
43	298470	336	Drugbank (DB06608)
687800	1292	600	Drugbank (DB00845)
8	76	960	Drugbank (DB00608)
689758	376488	3960	Drugbank (DB08903)

Appendix H

SPICE simulations

A new readout platform for EIS measurements of NTS viability was presented in this work. In the platform, an operational amplifier in transimpedance configuration (OPA858) was employed. The circuitual model of the platform, complemented by a voltage generator and the solution resistance, is reported in Fig. H.1. The transfer function of the circuit, computed by taking as input the current from the DUT and as output the voltage to be sampled by the ADC, is reported in Fig. H.2B. An accurate estimation of the transfer function above 1 MHz would require a deeper characterization of the parasitic capacitances on the PCB and is not of interest to this work. The expected overall noise level of electronic components on the PCB featuring the transimpedance amplifier is reported in Fig. H.2A.

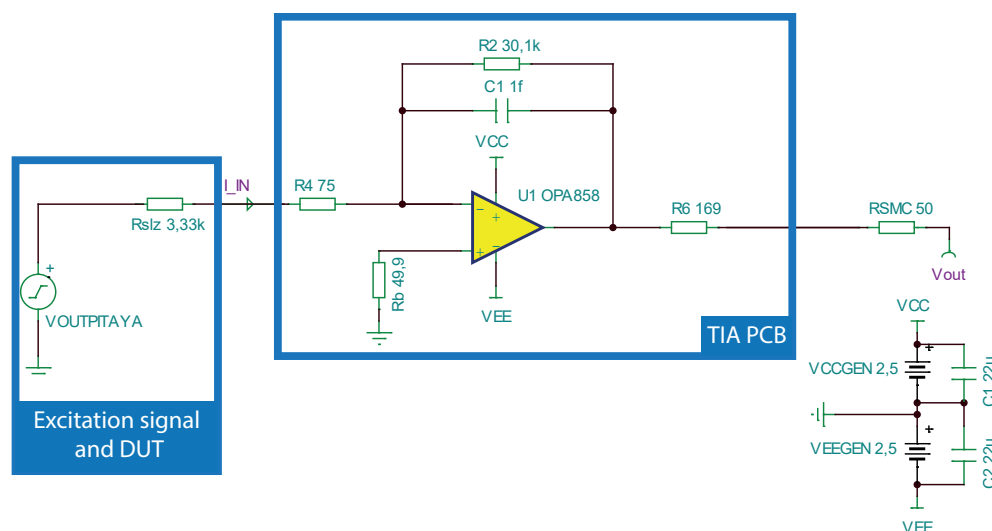


Figure H.1. Schematic of the TinaTI™ model.

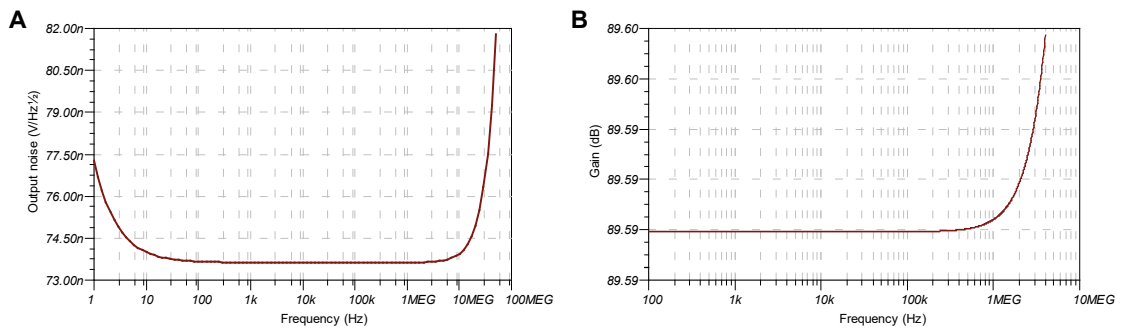


Figure H.2. A) Output noise spectrum. B) Trans-impedance gain as function of input frequency.

Bibliography

- [1] Paolo S. Ravaynia et al. «Parallelized Impedance-Based Platform for Continuous Dose-Response Characterization of Antischistosomal Drugs». In: Advanced Biosystems 4.7 (2020), pp. 1–12. ISSN: 23667478. DOI: [10.1002/adbi.201900304](https://doi.org/10.1002/adbi.201900304).
- [2] SCI Foundation. Schistosomiasis. URL: <https://schistosomiasiscontrolinitiative.org/ntds/parasitic-worms/schistosomiasis>.
- [3] Daniel G Colley et al. «Human schistosomiasis». In: The Lancet 383.9936 (2014), pp. 2253–2264. DOI: [10.1016/S0140-6736\(13\)61949-2](https://doi.org/10.1016/S0140-6736(13)61949-2).
- [4] WHO EMRO. Schistosomiasis: Details. URL: <https://www.who.int/news-room/fact-sheets/detail/schistosomiasis>.
- [5] WHO EMRO. Schistosomiasis. URL: <http://www.emro.who.int/health-topics/schistosomiasis/introduction.html>.
- [6] Gordana Panic et al. «Activity profile of an FDA-approved compound library against *Schistosoma mansoni*». In: PLoS Neglected Tropical Diseases 9.7 (2015), pp. 1–15. ISSN: 19352735. DOI: [10.1371/journal.pntd.0003962](https://doi.org/10.1371/journal.pntd.0003962).
- [7] Emmanuel Mouafo Tekwu et al. «Mechanically produced schistosomula as a higher-throughput tools for phenotypic pre-screening in drug sensitivity assays: Current research and future trends». In: 4.1 (Dec. 2016), p. 21. DOI: [10.1186/s40364-016-0075-2](https://doi.org/10.1186/s40364-016-0075-2).
- [8] David C. Swinney. «Molecular Mechanism of Action (MMoA) in Drug Discovery». In: Annual Reports in Medicinal Chemistry. Vol. 46. Academic Press Inc., Jan. 2011, pp. 301–317. DOI: [10.1016/B978-0-12-386009-5.00009-6](https://doi.org/10.1016/B978-0-12-386009-5.00009-6).
- [9] Robert A Copeland, David L Pompliano, and Thomas D Meek. «Drug-target residence time and its implications for lead optimization». In: Nature Reviews Drug Discovery 5.9 (2006), pp. 730–739. ISSN: 14741784. DOI: [10.1038/nrd2082](https://doi.org/10.1038/nrd2082).
- [10] Lalit Kumar Sharma et al. «Design and synthesis of molecular probes for the determination of the target of the anthelmintic drug praziquantel». In: Bioorganic and Medicinal Chemistry Letters 24.11 (2014), pp. 2469–2472. ISSN: 14643405. DOI: [10.1016/j.bmcl.2014.04.014](https://doi.org/10.1016/j.bmcl.2014.04.014).

- [11] Paul McCusker et al. «Non-sedating benzodiazepines cause paralysis and tissue damage in the parasitic blood fluke *Schistosoma mansoni*». In: *PLOS Neglected Tropical Diseases* 13.11 (Nov. 2019), pp. 1–17. DOI: [10.1371/journal.pntd.0007826](https://doi.org/10.1371/journal.pntd.0007826).
- [12] Reem Osama A. Kamel and Fatma El Zahraa Anwar Bayaomy. «Ultrastructural alterations in *Schistosoma mansoni* juvenile and adult male worms after in vitro incubation with primaquine». In: *Memorias do Instituto Oswaldo Cruz* 112.4 (2017), pp. 247–254. ISSN: 16788060. DOI: [10.1590/0074-02760160324](https://doi.org/10.1590/0074-02760160324).
- [13] Francesca Stradolini. «IoT Bio-Electronic Multi-Panel Device for On-line Monitoring of Anaesthesia Delivery». In: (2018), p. 216. DOI: [10.5075/epfl-thesis-8800](https://doi.org/10.5075/epfl-thesis-8800).
- [14] Kenneth E Thummel, Danny D Shen, and Nina Isoherranen. «Design and Optimization of Dosage Regimens: Pharmacokinetic Data». In: *Goodman & Gilman's: The Pharmacological Basis of Therapeutics*, 13e. Ed. by Laurence L Brunton, Randa Hilal-Dandan, and Björn C Knollmann. New York, NY: McGraw-Hill Education, Nov. 2017. URL: <http://accessmedicine.mhmedical.com/content.aspx?aid=1172428294>.
- [15] Ross A. Paveley et al. «Whole Organism High-Content Screening by Label-Free, Image-Based Bayesian Classification for Parasitic Diseases». In: *PLoS Neglected Tropical Diseases* 6.7 (July 2012). Ed. by Anton Simeonov, e1762. ISSN: 1935-2735. DOI: [10.1371/journal.pntd.0001762](https://doi.org/10.1371/journal.pntd.0001762).
- [16] Theresia Manneck et al. «Isothermal microcalorimetry to study drugs against schistosoma mansoni». In: *Journal of Clinical Microbiology* 49.4 (Apr. 2011), pp. 1217–1225. ISSN: 00951137. DOI: [10.1128/JCM.02382-10](https://doi.org/10.1128/JCM.02382-10).
- [17] Mario M. Modena et al. «Impedance-based detection of *Schistosoma mansoni* larvae viability for drug screening». In: vol. 2018-January. c. 2018, pp. 1–4. ISBN: 9781509058037. DOI: [10.1109/BIOCAS.2017.8325227](https://doi.org/10.1109/BIOCAS.2017.8325227).
- [18] Sandro Carrara. *Bio/CMOS interfaces and co-design*. Vol. 9781461446903. Springer New York, Oct. 2013, pp. 1–258. ISBN: 9781461446903. DOI: [10.1007/978-1-4614-4690-3](https://doi.org/10.1007/978-1-4614-4690-3).
- [19] makyzz /FreePik. Oct. 2020. URL: https://www.freepik.com/free-vector/target-icon-business-sport_1250656.htm.
- [20] Eric K Sackmann, Anna L Fulton, and David J Beebe. «The present and future role of microfluidics in biomedical research». In: *Nature* 507.7491 (2014), pp. 181–189. DOI: [10.1038/nature13118](https://doi.org/10.1038/nature13118).
- [21] DNDi et al. MMV. *Pandemic Response Box*. URL: <https://www.mmv.org/mmv-open/pandemic-response-box/about-pandemic-response-box>.
- [22] David S. Wishart et al. «DrugBank 5.0: A major update to the DrugBank database for 2018». In: *Nucleic Acids Research* 46.D1 (Jan. 2018), pp. D1074–D1082. ISSN: 13624962. DOI: [10.1093/nar/gkx1037](https://doi.org/10.1093/nar/gkx1037).

- [23] Benjamin M. Bolker. *Ecological Models and Data in R*. Princeton University Press, 2008. ISBN: 9780691125220. DOI: [10.2307/j.ctvc4g37](https://doi.org/10.2307/j.ctvc4g37). URL: <http://www.jstor.org/stable/j.ctvc4g37>.
- [24] Eden Microfluidics. *Flexdym Supporting Document*. URL: <https://eden-microfluidics.com/support>.
- [25] Christian Lohasz et al. «A Tubing-Free, Microfluidic Platform for the Realization of Physiologically Relevant Dosing Curves on Cellular Models». In: vol. 1. 4. MDPI AG, Sept. 2017, p. 497. DOI: [10.3390/proceedings1040497](https://doi.org/10.3390/proceedings1040497). URL: <http://www.mdpi.com/2504-3900/1/4/497>.
- [26] Ludmila Boinovich and Alexandre Emelyanenko. «Characterizing the Physicochemical Processes at the Interface through Evolution of the Axisymmetric Droplet Shape Parameters». In: *Advances in Contact Angle, Wettability and Adhesion*. John Wiley & Sons, Ltd, 2018. Chap. 4, pp. 99–129. ISBN: 9781119459996. DOI: <https://doi.org/10.1002/9781119459996.ch4>.
- [27] Li Hong Zhao, Jennifer Lee, and Pabitra N. Sen. «Long-term retention of hydrophilic behavior of plasma treated polydimethylsiloxane(PDMS) surfaces stored under water and Luria-Bertani broth». In: *Sensors and Actuators, A: Physical* 181 (July 2012), pp. 33–42. ISSN: 09244247. DOI: [10.1016/j.sna.2012.04.038](https://doi.org/10.1016/j.sna.2012.04.038).
- [28] Joseph R Lakowicz et al. «Release of the self-quenching of fluorescence near silver metallic surfaces». In: *Analytical biochemistry* 320.1 (2003), pp. 13–20. DOI: [10.1016/S0003-2697\(03\)00351-8](https://doi.org/10.1016/S0003-2697(03)00351-8).
- [29] macrovector /FreePik. Oct. 2020. URL: https://fr.freepik.com/vecteurs-libre/microscope-scientists-round-concept_4029340.htm.
- [30] Moritz Lang, Fabian Rudolf, and Jörg Stelling. «Use of YouScope to implement systematic microscopy protocols». In: *Current protocols in molecular biology* 98.1 (2012), pp. 14–21. DOI: [10.1002/0471142727.mb1421s98](https://doi.org/10.1002/0471142727.mb1421s98).
- [31] Curtis T Rueden et al. «ImageJ2: ImageJ for the next generation of scientific image data». In: *BMC bioinformatics* 18.1 (2017), p. 529. DOI: [10.1186/s12859-017-1934-z](https://doi.org/10.1186/s12859-017-1934-z).
- [32] Lukas Novotny and Bert Hecht. «Quantum emitters». In: *Principles of Nano-Optics*. 2nd ed. Cambridge University Press, 2012, pp. 282–312. DOI: [10.1017/CB09780511794193.011](https://doi.org/10.1017/CB09780511794193.011).
- [33] J Keiser. «In vitro and in vivo trematode models for chemotherapeutic studies». In: *Parasitology* 137.3 (2010), pp. 589–603.
- [34] Sh. Kogan. «1/f noise and random telegraph noise». In: *Electronic Noise and Fluctuations in Solids*. Cambridge University Press, 1996, pp. 203–286. DOI: [10.1017/CB09780511551666.009](https://doi.org/10.1017/CB09780511551666.009).

- [35] Ameteksi SI. What is a Lock-in Amplifier? URL: https://www.ameteksicom/-/media/ameteksicom/download_links/documentations/7210/tn1000_what_is_a_lock-in_amplifier.pdf.
- [36] GA Stimpson et al. «An open-source high-frequency lock-in amplifier». In: *Review of Scientific Instruments* 90.9 (2019), p. 094701. DOI: [10.1063/1.5083797](https://doi.org/10.1063/1.5083797).
- [37] Rob Campbell. Matlab file exchange: shadedErrorBar. Oct. 2020. URL: <https://github.com/raacampbell/shadedErrorBar>.
- [38] Brian Kirby. *Micro- and Nanoscale Fluid Mechanics*. 2010th ed. Cambridge: Cambridge University Press, 2010. ISBN: 9780521119030. DOI: [10.1017/CB09780511760723](https://doi.org/10.1017/CB09780511760723).
- [39] G. K. Batchelor. «Flow of a Uniform Incompressible Viscous Fluid». In: *An Introduction to Fluid Dynamics*. Cambridge Mathematical Library. Cambridge University Press, 2000, pp. 174–263. DOI: [10.1017/CB09780511800955.006](https://doi.org/10.1017/CB09780511800955.006).
- [40] Henrik Bruus. «Theoretical microfluidics». In: *Choice Reviews Online* 45.10 (2008), pp. 45–5602–45–5602. ISSN: 0009-4978. DOI: [10.5860/choice.45-5602](https://doi.org/10.5860/choice.45-5602).
- [41] Alvaro Mata, Aaron J Fleischman, and Shuvo Roy. «Characterization of Polydimethylsiloxane (PDMS) Properties for Biomedical Micro/Nanosystems». In: 7.4 (2005), pp. 281–293. DOI: [10.1007/s10544-005-6070-2](https://doi.org/10.1007/s10544-005-6070-2).
- [42] Mehdi Mortazavi and Michael Nosonovsky. «A model for diffusion-driven hydrophobic recovery in plasma treated polymers». In: *Applied Surface Science* 258.18 (July 2012), pp. 6876–6883. ISSN: 01694332. DOI: [10.1016/j.apsusc.2012.03.122](https://doi.org/10.1016/j.apsusc.2012.03.122).
- [43] Tony J. Roupael. «Nyquist-Rate Data Conversion». In: *Signal Processing for Software-Defined Radio*. Newnes, Jan. 2009. Chap. Chapter 8, pp. 235–277. DOI: [10.1016/b978-0-7506-8210-7.00008-4](https://doi.org/10.1016/b978-0-7506-8210-7.00008-4).

List of abbreviations

The following table summarizes the abbreviations used in this thesis. The page where the abbreviation is first used and/or defined is also provided.

Abbreviation	Meaning	Page
AC	Alternating current	8
ADC	Analog-to-digital converter	28
ADME	Absorption, Distribution, Metabolism and Excretion	5
AIC	Akaike Information Criterion	13
BNC	Bayonet Neill-Concelman	29
ChEMBL	Chemicals from European Molecular Biology Laboratory	77
CPE	Constant Phase Element	8
DAC	Digital-to-analog converter	28
DC	Direct current	27
DDS	Direct digital synthesis	30
DMSO	Dimethyl sulfoxide	39
DUT	Device under test	28
EIM	Electrical-impedance microwell	7
EIS	Electrochemical Impedance Spectroscopy	1
ETH	Eidgenössische Technische Hochschule	8
FITC	Fluorescein isothiocyanate	20
FPGA	Field Programmable Gate Array	28
IMC	Isothermal microcalorimetry	7
LPCVD	Low Pressure Chemical Vapour Deposition	18
MCLZ	Meclonazepam	4
MF	Medium frequency	28
MMV	Medicines for Malaria Venture	77
NTD	Neglected tropical disease	2
NTS	Newly transformed schistosomulae	3
OXE	Oxethazaine	38
PCB	Printed circuit board	29

H – List of abbreviations

Abbreviation	Meaning	Page
PD	Pharmacodynamic	6
PDMS	Polydimethylsiloxane	19
PK	Pharmacokinetic	5
PMMA	Polymethyl methacrylate	15
PZQ	Praziquantel	2
RE	Reference electrode	8
RePLIA	Red Pitaya lock-in amplifier	30
SMA	SubMiniature version A	29
SoC	System on a chip	30
SPICE	Simulation Program with Integrated Circuit Emphasis	9
TIA	Transimpedance amplifier	28
UV	Ultraviolet	17
WE	Working electrode	9
WHO	World Health Organization	2
